Resistance de-welding of thermoplastic composites

Next step in sustainable joints

Maarten de Jong

University of Twente

nlr

Resistance de-welding of thermoplastic composites

Next step in sustainable joints

by

Maarten de Jong

Student Name	Student Number
Maarten Christiaan	2655748

Version	Date
V2.5 - Final	Monday 21st October, 2024

Supervisor:	DR.IR. W.J.B. Grouve
Supervisor company:	DR. O. Erartsin
Project Duration:	November, 2023 - October, 2024
Faculty:	Faculty of Production Technology, Enschede

Cover: Aircraft Flying in the Sunset by Gerhard Gellinger (Modified)

UNIVERSITY OF TWENTE.

NLR

Summary

Carbon-reinforced thermoplastic composites are increasingly used in the aerospace industry due to their lightweight properties and promising characteristics. These characteristics compromise fast processing times and recyclability enabled by the (re)-meltability of the thermoplastic matrix material [1]. Traditional thermoset composites require lengthy curing processes and cannot be remelted [2]. The thermoplastics's meltability allows for welding which can achieve fast processing cycles and reduces stress concentrations [3]. However, while significant research has been done on welding techniques, little attention has been given to disassembling these welded joints, a crucial process for maintenance, repair, and recycling in the aerospace industry. This thesis focuses on the disassembly of thermoplastic composites by first reheating the joint interface and applying forces to separate the bonded parts with minimal damage. In this thesis, this dissembling is referred to as "de-welding". De-welding is the reverse of the welding process.

The de-welding in this thesis focused on resistance heating as the heating method, as it directly heats the joint interface, reducing the heat-affected zone to avoid damage in the composite adherends. Moreover, the heating element remains in the joint, which is advantageous for reprocessing. The main objective of this research was to assess the feasibility of de-welding thermoplastic composites using resistance heating. More specifically, with a woven carbon fiber as the heating element and carbon fiber-reinforced low-melting poly-aryl-ether-ketone (CF/LMPEAK) adherends. The feasibility was evaluated through numerical modeling and experimental tests on two geometries: coupon-sized specimens and larger structural elements. For the latter, an experimental test bench was developed.

The predictive numerical model successfully captured the heating behavior by measuring validation. The model also showed that using a heat sink at the boundary of the laminate surfaces and a glass fiber layer significantly affected the through-thickness heating behavior. The results of the coupon-sized specimens showed that de-welding via resistance heating is a feasible method for lowering the disassembly force. These specimens used a PEI interlayer, enabling processing temperatures below the melt temperature of the LMPEAK adherends and so keeping the adherends intact. When applied to all LMPEAK, larger structural elements, de-welding successfully achieved low disassembly force, no de-consolidation, and an intact heating element. These outcomes were obtained by applying a heat sink, a glass insulator layer, and a relatively short processing time. The specimens were rapidly heated to melt temperatures at the interface, resulting in almost zero-strength remaining.

This thesis took the first step in de-welding by resistance heating by showing the feasibility of the process. The heat sinks showed great cooling rates but made the process quite energy-demanded. More research is required to develop this disassembly technique into a qualified manufacturing process in the aviation industry.

Contents

Nomenclature

Abbreviations

Abbreviation	Definition
CFRP	Carbon fiber reinforced polymer
TPC	Thermoplastic composite
FLIR	Infrared camera
LSS	Lap shear strength
RT	Room temperature
st. dev.	Standard deviation
TC	Thermocouple
TC1	Interface thermocouple
TC2	Surface thermocouple

Symbols

Symbol	Definition	Unit
A	Cross-sectional area	[m^2]
A_i	Cross-sectional area of the ith layer	[m^2]
cp	Specific heat capacity at constant pressure	[J/kg·K]
I	Excitation current	[A]
J	Current density	[A/m^2]
k	Thermal conductivity	[W/m·K]
l	Path length of heat or current	[m]
lo	Overlap length of the joint	[m]
Q	Heat of a heat element	[J]
P	Power density of a heat source	[W/m^2]
R	Electrical resistance	[Ω]
α	temperature-resistance coefficient	[1/K]
$R_{thermal}$	Thermal resistance	[K/W]
T	Temperature	[°C]
T_g	Glass transition temperature	[°C]
T_m	Melt temperature	[°C]
V	Voltage	[V]
v_f	Fibre volume fraction	[-]
v_m	Matrix volume fraction	[-]
w_f	Weight fraction of the fibres	[-]
w_o	Overlap width of the joint	[m]
ϵ	Emissivity	[-]
ρ	Density	[kg/m^3]

1

Introduction

This introduction begins with a brief overview of thermoplastic composites and their application in aircraft structures. Then, the problem is described, followed by an outline of the objective and scope of this thesis.

1.1. Background

The aviation industry is under significant pressure to transition towards sustainability rapidly. To achieve this goal, the industry is pursuing approaches such as reducing waste in production, focusing on more recyclable materials, and more lightweight constructions. Concerning the latter, significant gains have already been made over the past decades with the introduction of composite materials. For example, the Boeing 787 Dreamliner is constructed with these lightweight composites, 80 % composite by volume and 50% by weight, showcasing their excellent weight per strength ratio (Fig.1.1). As the number of flights and aircrafts are anticipated to increase, there is a growing demand for lightweight materials, allowing for fast and affordable manufacturing, that also can be recycled [4].

Nowadays, the aircraft industry primarily uses composites with a thermoset matrix polymer. The manufacturing of these thermoset composites is time-consuming due to the necessary curing process. Furthermore, once the thermoset composites have solidified, they cannot be remelted, ruling out the possibility of (post) processing like welding and posing challenges for end-of-life recycling. Thermoplastics composites do not require such a curing step and also exhibit other advantages such as (re)-melting allowing for welding, repairing, and recycling [1].

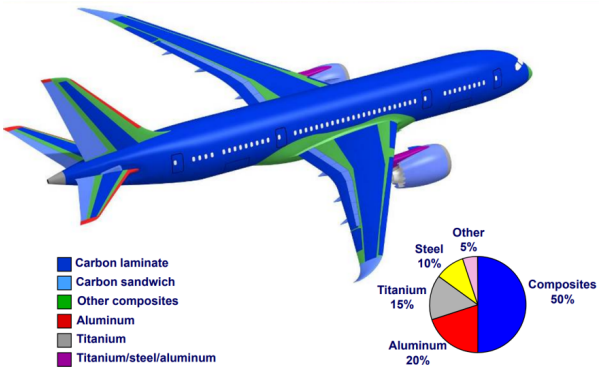

Figure 1.1: Material overview of the Boeing 787 [5]

Thermoplastic composites (TPCs) offer the possibility to be fusion bonded, facilitated by the meltability of the thermoplastic matrix material [1]. This process, also known as welding, presents a significant im-

provement over traditional methods used for joining metal and thermoset composite assemblies, such as mechanical fastening and adhesive bonding. Compared to fusion bonding, mechanical fastening requires additional manufacturing steps, adds weight and induces stress concentrations at the vicinity of the holes in the material [6]. Adhesive bonding requires longer manufacturing cycles, compared to the short processing times achievable with welding. By enabling fusion bonding, TPCs can overcome the limitations of mechanical fasteners and adhesive bonding, potentially resulting in lighter, more efficient assemblies. However, the welding of TPCs does require higher manufacturing temperatures [7]

Figure 1.2: Demonstration of a thermoplastic fuselage section, showing a welded stiffened panel.[8]

The welding technologies for thermoplastic composites in aircraft are getting mature and some welded structures are certified to fly. An example of a future aircraft thermoplastic component is shown in Figure 1.2. This figure depicts an entirely thermoplastic assembly of stiffeners on a fuselage section, as demonstrated by DLR. In this assembly, C-shaped stiffeners are resistance welded onto the fuselage skin, replacing mechanical fasteners and reducing weight [9]. Aircraft stiffeners, often called frames, are essential to prevent bending (horizontal stiffeners) and buckling (transverse stiffeners), and so maintaining the fuselage's shape [10]. As illustrated, these stiffeners can nowadays be attached to the fuselage skin using welding techniques, allowing for excellent load transfer in the weld zone between the stiffener and skin.

However, if these structures are not positioned correctly or reach the end of their lifecycle, they must be disassembled. The process for disassembling thermoplastic composites is yet unclear and is a new field to explore.

1.2. Problem statement

Despite ongoing research into welding techniques for TPCs, research on the disassembly of fusion-bonded joints remains limited. In order to fully utilize TPCs in aircraft structures, it is essential to establish a systematic approach for their repair and maintenance [1]. Effective disassembling strategies can offer the prospect of repositioning the welded parts due to assembly errors or removing a damaged part for repair or recycling, contributing to more sustainable manufacturing and assembly of aerospace components [7]. The next step in sustainable manufacturing is to "de-weld". Which is a novel disassembly process with the following definition:

> *De-welding refers to the reverse of the "welding" process in which the thermoplastic fusion bond between the welded parts is removed by first heating the interface and subsequently applying de-welding forces.*

A 'good' deweld (disassembly by de-welding) is fulfilled by achieving the following requirements:

- No delamination in the adherends
- Low de-weld/disassembly force

- Intact heating element

One viable and promising option to facilitate de-welding is reheating of the joint to lower the required disassembly force, showed by the studies of De Weert [11] and Frederick [12]. Theoretically, fusion-bonded joints could be reheated to soften the joint and lower the force required for disassembly. It would be useful to localize this heating into the joint interface, to limit the extent of the heat-affected zone, which could negatively affect the composites adherends properties.

Heating at the interface can be achieved using different techniques such as induction, microwave, or resistance heating. When using induction or microwave heating, the carbon fiber-reinforced adherends themselves are heated, making it challenging to concentrate the heat precisely at the interface [11, 12]. This may result in the deconsolidation of the adherends, a phenomenon where the layers of the composite material begin to separate, thereby undermining the structural integrity of the material.

To overcome these challenges, resistance heating is selected as the preferred heating mechanism, as it generates heat exactly at the joint interface, regardless of the material, layup, or thickness of the adherends, by using a heating element. This minimizes the extent of the heat-affected zone, thus preserving the integrity of the adherends while facilitating efficient disassembly. However, using a heating element, its ends must be accessible within an assembly for reheating. NLR [13] performed some de-welding experiments on coupon-sized levels, showcasing the practical feasibility. The next step is to deepen this research and improve the de-welding process to larger structural elements, shown in Figure 1.3.

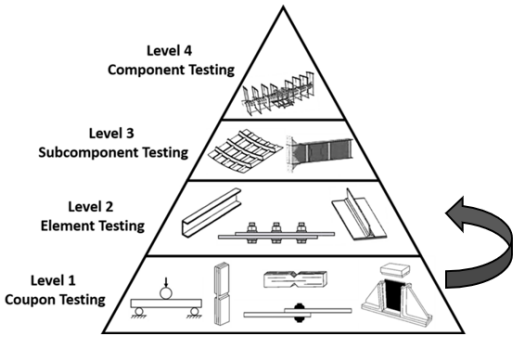

Figure 1.3: The next phase for the de-welding manufacturing process, picture adapted from [14]

1.3. Research objective & scope Thesis

Following the problem statement in the previous section, the research objective of this graduation assignment is to assess the feasibility of the de-welding process of thermoplastic composites by means of resistance heating. The feasibility is checked by analyzing numerically and experimentally the de-welding behavior of carbon-reinforced low-melting Poly-Aryl-Ether-Ketone (CF/LMPEAK) for two types of geometries, namely coupon-sized and element-sized.

First, the resistance heating process is characterized, focusing on identifying critical parameters. Then, a predictive numerical model is developed to analyze the de-weld process. The model is validated through experimental heating tests.

The experimental phase is performed in two stages: first, coupon-sized specimens are tested using a standardized method. Second, the experimental research is extended to element-sized specimens tested in a developed test bench.

1.4. Outline Thesis

Following the objective defined in the previous section, the outline of this thesis is as follows. The thesis starts with a review in Chapter 2 on thermoplastic composites in the aviation industry, resistance welding, and disassembly strategies. Also, useful testing methodologies and evaluation procedures are described. In Chapter 3, the developed test bench for de-welding is explained. Chapter 4, the research methodology, with all the materials, experiments, and FEM model, is described. The test results are discussed in Chapter 5, and conclusions are drawn in Chapter 6, with recommendations for further research.

2

Literature review

This chapter presents the relevant literature on the disassembly of thermoplastic joints. First, the general thermoplastic composites in aviation are evaluated. Followed by the fusion bond process and the resistance welding process. Then, the disassembly/repair/opening of thermoplastic composites is reviewed. Finally, relevant testing and analyse procedures are described.

2.1. Thermoplastic composites in aviation

In the last decade, the transition from thermoset to thermoplastics has begun [9]. TPCs are composed of fibers embedded in a thermoplastic polymer matrix. These fibers give the composite the most strength. At the same time, the lighter matrix polymers protect the fibers, hold them together, and facilitate load transfer between them [15]. Thermoset resins have a rigid three-dimensional network structure. Thermoplastic matrices have individual molecules held in place by Van der Waals, hydrogen, and weak secondary bonds [16].

Polymers

The most common thermoplastics of use in the aviation industry are listed in table 2.1, with their molecular arrangement (*i.e.* amorphous or semicrystalline). In amorphous polymers, the chains are arranged randomly, while in crystalline materials, the molecules are aligned in regular and repeating patterns. As shown in Fig. 2.1, a portion of semi-crystalline thermoplastic exhibits a structured arrangement. This fraction depends on processing parameters, mainly on cooling rate, and significantly influences the final properties of the composite [17].

Figure 2.1: Polymer arrangements: amorphous (left) and semi-crystalline (right), picture adopted from [15].

The PAEKs (PolyArylEtherKetones) polymers are the standard in aerospace composites, including PEKK/PAEK/PEKEKK polymers. The best-known PAEK is PEEK (poly-ether-ether-ketone), a semi-crystalline polymer with good chemical resistance, fatigue, creep and wear properties [5, 18]. Below in Table 2.1, the most commonly used thermoplastics are listed.

In the quest for faster processing times, one option is to lower the processing temperature. The process temperature typically lies 30-50 °C above the melting temperature for (semi)-crystalline polymers and

the glass temperature for amorphous polymers. Victrex© developed a new PAEK polymer, named LM-PAEK (Table 2.1), with a reduced T_m while retaining the T_g and hence keeping the high-temperature properties [19].

Material	T_g(°**C**)	T_m(°**C**)	**Crystallinity**
PEEK	134-158	334-350	16%-47%
PEKK	134-158	334-350	16%-47%
PAEK	134-158	334-350	16%-47%
LM-PEAK	134-158	305	16%-47%
PEI	217	-	amorf
PPS	85	285-295	40%-83%

Table 2.1: properties of used thermoplastics in aerospace structures [16]

Fibers
In the aerospace industry, commonly used composites are made of a polymer matrix reinforced with glass or carbon fibers. Carbon Fiber Reinforced Polymers (CFRPs) are favored over glass fiber composites due to their high specific stiffness in the axial direction. Carbon fibers are also corrosion-resistant, unlike some metals, making CFRPs suitable for use in harsh environments, such as at high altitudes, in marine settings, and in chemical environments. Carbon fibers are electrical conductive [9].

2.2. Fusion bonding of TPCs

Stavrov et al. [20] broadly defined fusion bonding as the joining of two polymer parts that uses the ability of thermoplastic matrices to flow when heated beyond their glass transition temperature T_g (for amorphous polymers) or the crystalline melting point T_m (for semi-crystalline polymers). During the process, heat and pressure are applied to thermoplastic part surfaces, allowing for molecule diffusion and eventually consolidation [21]. This process is illustrated in Fig. 2.2. Initially, two composite laminates are placed on top of each other under pressure, establishing initial surface contact. As the temperature increases, the viscosity decreases, allowing the polymer chains at the interface to begin partially diffusing into each other. Intimate contact (second phase of Fig. 2.2) is established when the barriers caused by irregularities at the interface are suppressed, allowing molecular chains to move freely across the interface in the process of inter-diffusion, also known as autohesion [22]. After a period of inter-diffusion the heating is stopped and the material cools down. The matrix solidifies under applied pressure, leading to complete diffusion between the laminates. For semi-crystalline polymers, crystallization happens after the solidification and between the T_m and T_g cool-down region. With the right combination of time, pressure, and heat, this process produces a strong and cohesive bond [5, 7].

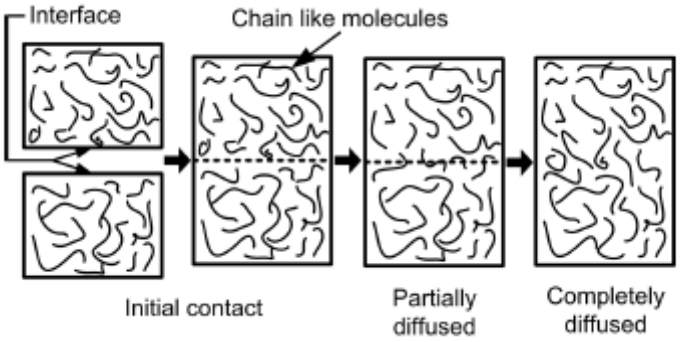

Figure 2.2: Fusion bonding process [3]

Multiple joining techniques have been developed to join unreinforced and reinforced thermoplastic polymers. These fusion bond techniques (also referred to as welding techniques) are categorized in Figure 2.3. Each welding technique has its advantages and pitfalls. In the remaining section, resistance welding, an electromagnetic heating strategy, is explained further.

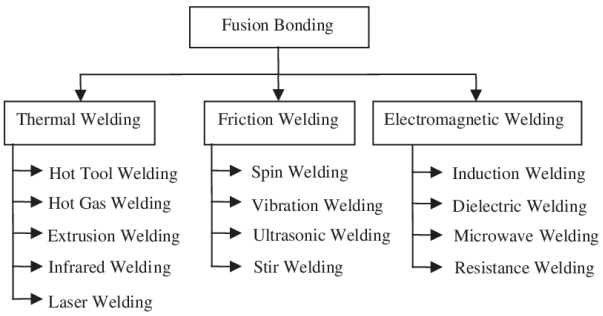

Figure 2.3: Overview fusion bond techniques [22]

De-welding
As outlined in the introduction, the de-welding process is essentially the fusion bond process reversed. To achieve an effective de-weld, the following steps must occur based on the process shown in Fig. 2.2:

- Heat application: The bond, which consists of fully diffused material, must be heated in a controlled manner at the desired separation location.
- Partial diffusion: As the temperature rises, the viscosity of the matrix material decreases locally, softening the interface. The increase in temperature should remain limited in the adherends.
- Separation: At the melt temperature T_m, the molecular chains at the interface become mobile. When disassembly forces are applied, these chains should remain intact, allowing the laminates to separate cleanly with low forces. If the interface is sufficiently molten, minimal force will be required to complete the separation.

2.3. Resistance heating/welding

In Chapter [5], it was described that disassembly via resistance heating can be a viable option. When resistance heating is applied for fusion bonding purposes, it is called resistance welding. In this section, the resistance welding process is reviewed.

2.3.1. Weld process

Resistance welding uses an electrically resistive element to generate heat at the interface between the joint adherends. An electrical current is applied to the resistive element, which locally heats and melts the polymer around the element [1]. The power (heat) dissipated from the element is proportional to the current and resistance; P (heat) is given by Joule's Law (resistive heating):

$$P = I^2 R \tag{2.1}$$

where I is the current and R is the electrical resistance. As the formula shows, the resistance value of the heating element directly influences the heat input at the weld interface and, subsequently, the temperature at this location.

When the temperature at the bond, or so-called interface, rises to the melt temperature of the thermoplastic due to resistive heating, welding begins under the application of pressure. The welding pressure ensures intimate contact, allowing the fusion bonding process, explained in Section 2.2, to occur. The temperature, pressures, and duration influence the strength and quality of the weld [23]. Figure 2.4 shows a schematic of the resistance welding process; below the figure, the parts are individually elaborated.

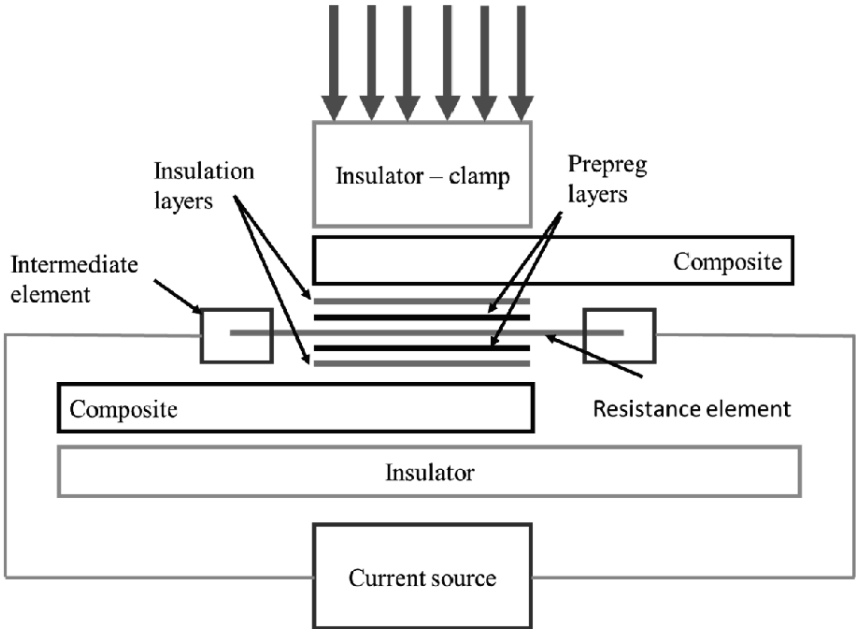

Figure 2.4: Schematic of resistance welding [24]

Resistance element (Heating element): This part provides heat by Joule heating. The heating element can be made out of different materials. The materials in the literature are carbon fibers, stainless steel, and multi-walled carbon nanotubes. Carbon fiber heating elements are lightweight and compatible with the adherend but offer issues with repeatability due to clamping. A metal heating element, mostly stainless steel mesh, is less sensitive to clamping pressure and has thus a larger process window [7]. Lastly, multi-walled carbon nanotubes (MWCNTs) are a novel heating element with high flexibility to join complex structures [2]. Ageorges et al. [25, 22] conducted comparative studies between UD and fabric carbon fiber heating elements. The temperature distribution uniformity was better for the fabric element caused by the fiber's two directions. This resulted in significantly higher lap shear strength and interlaminar fracture toughness.

Intermediate element: Also known as the clamping component, this part applies pressure to minimize contact resistance while delivering electrical current. Stavrov [20], noted that sufficient clamping pressure is achieved with 4 to 20 MPa for carbon fiber and 2 MPa for stainless steel mesh heating elements.Ageorges [25] and Shi [26] noted that a low scatter (deviation) ,governed by varying contact resistance, can be minimized by a clamping pressure above 1MPA.

Insulation layers: Insulation is crucial for preventing current leakage, a significant challenge when welding carbon fiber laminates. Current leakage occurs when the highly conductive carbon fibers in the adherends contact those in the heating element, causing the entire weld stack to act as a heating element. The easiest way to solve this problem is using an electrical insulator around the heating element, such as a glass fiber layer [7]. However, this introduces a new material in the composite, with possible decrease strength and increased thickness [20].

Neat polymer layers: These optional resin layers can be applied to improve the quality of the bond. In the research of Hou et al. [27], the additional layers of raw thermoplastic complement the rough surface and provide a larger amount of material to the mutual diffusion process. As a result, it was noted to achieve up to 30 % more durable bond.

Insulator: This component presses the weld stack and is critical in thermal management. Talbot's study [28] highlighted the significant impact of different tooling materials on the through-thickness temperature gradient and interface temperature. When using tooling which extracts too much heat, the necessary temperature in the bond line cannot be achieved.

2.3.2. Process parameters

The power density is one of the most important parameters regarding the resistance weld process. The parameter is calculated by dividing the power, as described joules law in formula 2.1, by the area of the heating element. When applying a constant this results in the following power density formula (neglecting power losses from circuit losses):

$$P = \frac{UI}{lw} = \frac{V^2/R}{lw} \quad [\text{W/m}^2] \tag{2.2}$$

where U, the electrical voltage put into the heating element;I, the electrical current; R, the resistance of the heating element; l, length of the welded area $[m]$; w, width of the welded area $[m]$. Stavrov et al. [20] generally divided the power densities into three groups; low (10–75 kW/m2), intermediate (75–130 kW/m2), and high power level (from 130 kW/m2 upwards).

As formula 2.2 shows, the resistance value of the heating element has a direct influence on the temperature development at the weld interface. Multiple researchers [16, 12], noted that this parameter is critical and so favorable to calculate or measure, also at elevated temperatures. For most materials, electrical resistivity changes with temperature. A typical conductor's resistivity increases proportionally to the temperature with a linear relationship. This proportionality is called the resistance-temperature coefficient (α), which is positive for most metals but negative for carbon fibers [29].

In this research, a carbon fiber woven is used; multiple researchers noted that the carbon fiber heating element is not temperature-independent; it decreases as temperature increases [16, 12]. Ageorges [25] noted a linear decrease of 10% at 340°C for a woven C/PEEK heating element (25*160mm). DLR's study noted a reduction of 10% for the same material but longer heating element (25*260mm).

In the study by [30], two methods for controlling weld temperature were described, as shown in Figure 2.5.

- Supplying a constant current, voltage, or power over a set period of time. This method leads to a progressively rising temperature profile, followed by the cooling phase, which usually begins when the power source is turned off.
- Gradual adjustment of the current,voltage or power to maintain a stable temperature zone.

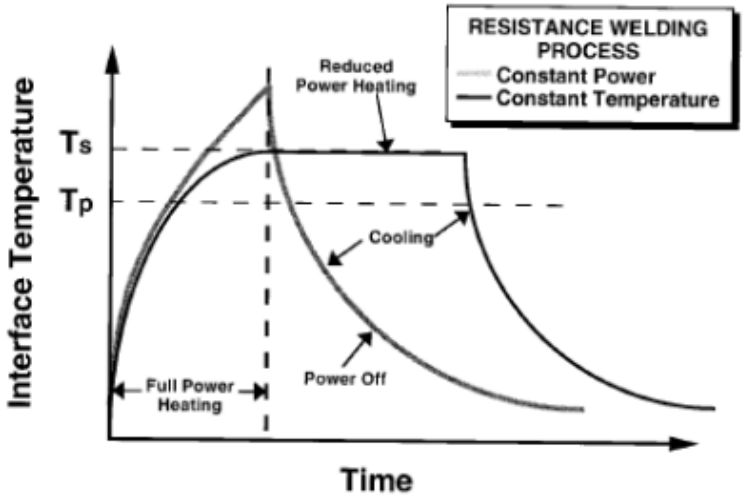

Figure 2.5: Two strategies of interface temperature control during resistance welding [31]

Edge effect
Ageorges et al. [21] pointed out that overheating due to exposure to air by natural convection is an important aspect of the resistance weld process. This effect is called the ”edge effect”, resulting from poor heat transfer at the edges of the weld, leading to a more rapid increase in temperature at this location [20]. In the study of Hou et al. [17], the melt propagation was analyzed, and it was shown that the edge effect directly influences the melting, as shown in Fig. 2.6. Because heat transfer near the edges is less efficient compared to the conduction within the laminates, the melting starts at the edges from the power input. Consequently, overheating and burning can happen before welding can start, i.e., making it challenging to control the temperature distribution between the $T_{melt} - T_{degradation}$ boundaries [32].

To reduce the edge effect, M.Endrass [8], and E.Talbot [28] noted that optimizing the clamping distance can minimize this. For longer welds, the non-uniformity can be improved by continuous or sequential resistance welding.

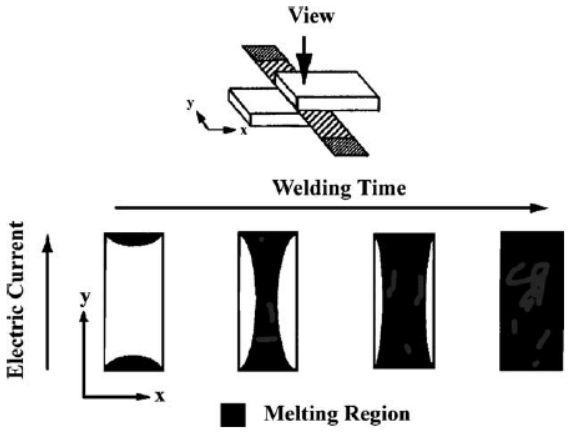

Figure 2.6: Schematic melting propagation flow [17]

2.3.3. Temperature control
A crucial aspect of the resistance weld process is the control and predictability of the interface temperature. Very useful hereby can be heat transfer modeling, where the heat equation can be solved in different manners: 1D 2D 3D, analytically, or numerically. When using a finite element code, conduction heat transfer coefficients, specific heat, and density of composite materials are needed [33]
However, thermal modeling is not always necessary, as experimental temperature data may be used to design a process window. Basically, there are two ways to control the resistance weld process, direct and indirect methods. The direct approach involves monitoring the temperature generated at the weld interface, which can be accomplished with the use of thermocouples. The study of Labrandero [34] noted some limitations of using thermocouples. First, thermocouples persist at the bond interface, acting as extra constituents that influence joint performance. Furthermore, it is important to electrically insulate (for example with Kapton tape) the thermocouples from the resistive heat element to avoid induced currents that could result in inaccurate measurements.

Another option is the indirect or closed-loop method. The temperature is predicted via modeling. The most straightforward way to monitor the temperature indirectly at the welding interface is by measuring the current and voltage of the heating element and following Ohm’s law. [35, 36]

2.4. Thermoplastic composites disassembly

In the thesis of de Weert [11], the feasibility of disassembly of carbon fiber / PEEK composites by induction welding was studied. Single-lap shear experiments were conducted by applying induction heating and showed that the disassembly force could be lowered significantly through this method. A reduction beyond 37% of the original lap shear strength was achieved. Induction welding was conducted with and without a susceptor, and significantly less energy was required with a steel metal mesh. As a consequence, the damage to the adherends could be limited. However, the inclusion of a susceptor lowers the joint strength. Thermal damage was located at the edges of the samples due to overheating. De Weert recommends that single lap shear tests may not be the best option for disassembly, and disassembly in peel might be easier and better. This is because fusion-bonded joints are less resistant to peel stresses than to shear stresses, as no fibers are aligned in that direction.

In the study of Frederick [12], ultrasonic welded SLS coupons were disassembled using resistance welding. This was carried out under a range of applied voltages in a tensile testing machine, leading to different temperatures at the joint interface (setup shown in figure 2.7). The behaviour of the joint during the disassembly was analyzed through shear stress and temperature curves. The thermoplastic used for the adherends is the same as for the bond line, namely polypropylene (PP). In general, this research showed the feasibility of using resistance welding for the first time in the literature as a disassembly method.

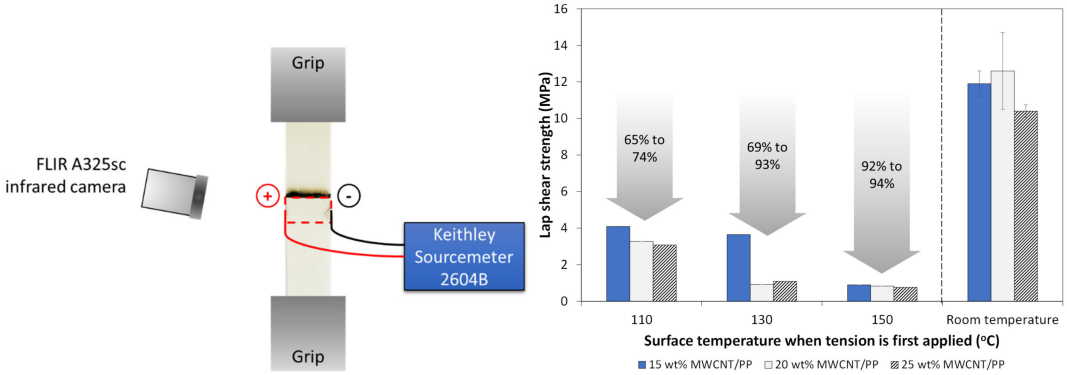

Figure 2.7: Study of [12], with Comparison between lap shear strength of GF/PP welded joints with resistance welding with multi-walled carbon nanotubes heating element

J. Barroeta Robles [16] conducted extensive research on the repair of thermoplastic composites. The review mainly covers the small-scale repair for damaged surfaces, which can recovered with a patch repair (like fixing your flat tire). Using an amorphous layer as an adhesive can lower the processing temperature. This solution is called the Thermabond^{TM} process, which will be discussed in the next section.

NLR studied the feasibility of disassembly of SLS-sized coupons by resistance welding. The materials and set-up were based on the studies of Endrass et al., from DLR [37, 23, 8]. A woven carbon fiber was used as the heating element, and the tests were conducted within a temperature range between the glass transition temperature Tg (143°C) and above melting point Tm (305°C + 30°C) of the LM-PAEK matrix material. The results showed that Heating to 180°C only slightly reduces the shear strength while higher temperatures cause a more drastic decrease. Heating to more than 300°C may drastically reduce the de-welding forces due to melt initiation in the LM-PAEK matrix. However, here the problems start with the flow of the matrix, resulting in losing the shape of the adherends.

Ageores et al., [25] noted the fact that by resistance welding, the implant stays in the composite, making it favorable for reprocessing/disassembly.

Thermabond process

Another option is using a polymer with a lower processing temperature at the joining interface. The characteristics of the interlayer polymer then allows the joining at a temperature below the melting temperature of the thermoplastic-reinforced adherends. This process is called Thermabond, or is known as dual polymer bonding [38, 20].In the studies of [39, 40, 41], the Thermabond process was taken advantage of by using the dual polymer PEI and PEEK. The miscibility of these polymers is really good, and results in a new process window depicted in Figure 2.8. The mechanical performance attain good, while the solvent resistance of the joint decreases to that of PEI, which has low chemical resistance. In the research of W. McLaughin [42], it was shown that a combination of amorphous and crystalline polymer improves the impact performances tremendously; in this study, it was tested with a PEI interlayer compared with a baseline CF/PEEK composite.

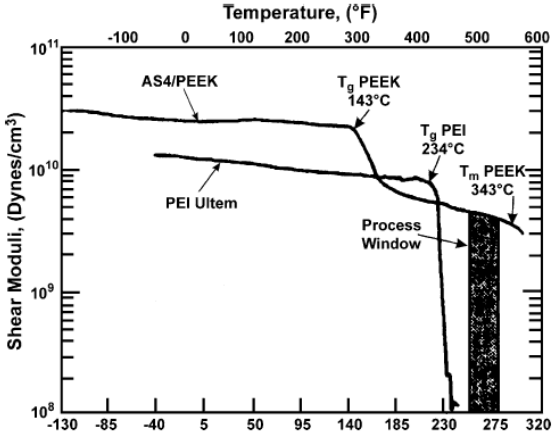

Figure 2.8: Thermabond process [39]

2.5. Testing and evaluation procedures

In the end, standard and simple equipment and procedures are necessary for in-field disassembly. This section discusses experimental testing and evaluation procedures for fusion-bonded joints. In this thesis single lap shear tests and pull-off tests are performed.

Single lap shear test

The lap shear test is the most commonly used experimental method for assessing joint quality in fiber-reinforced composites due to its simplicity [7]. The single lap shear test, Fig. 2.9(a), is also known as the thin lap shear test and is the standard tensile test of a welded specimen. Variants of this test are described in many standards, such as ASTM D 1002, ISO 4587, and ASTM D5868. [43]

Double cantilever beam test

The double cantilever bond test is used to test the out-of-plane properties of bonds. Stavrov [20], notes that this test is unreliable for resistance welded joints, often fiber bridging and cracking within the laminates were observed.

Pull-off test

Most studies on thermoplastic joint performance are on shear loading, and limited research is available for out-of-plane load applications. As discussed in section 2.4, directly pulling away the plates from each other appears to be the most logical option for disassembly purposes. There are no standardized tests available for pull-off loading of composites welds, but alternatively, in the literature of van Dijk [44], a set-up was developed to do so, shown in Fig. 2.9(c). Van Dijk importantly noted that the limitation of this setup is the asymmetric bending, attributed to the off-center stiffness from the L-shaped flange.

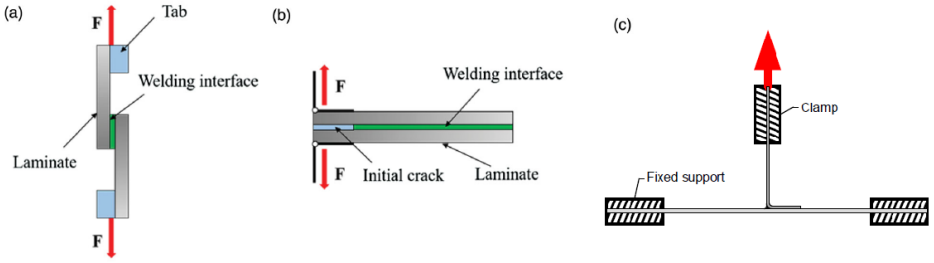

Figure 2.9: Test methods: (a) SLS configuration, (b) DCB configuration, and (c) L pull-off set-up. (Pictures adapted from [7, 44])

Analyzing failure mechanism

After mechanical testing of thermoplastics, different evaluation methods are their to analyze the failure modes and behaviour of the tested joint. Visual inspection of the fractured surfaces provides easy and quick feedback. The study of Ageorges [25] noted that in most cases, the fracture behavior is a combination of failures, with one being the most dominant.

Ultrasonic C-scan is a non-destructive testing method and can be utilized prior to mechanical testing to asses the quality of the weld. This technique provides valuable insights into the actual size of the welded area and detects irregularities within the weld. Another powerful method for evaluation is microscopy, which involves inspecting specimens to examine possible delamination.

2.6. Concluding remarks

This chapter describes the literature regarding the resistance heating and disassembly of fusion-bonded TPCs. It starts with a review of the materials used in the aviation industry, polymers and fibers, which allow aircraft structures to be fusion-bonded. The mechanisms playing a role in the fusion-bond process are outlined, along with how they relate to the de-welding process. Then, the resistance welding process was examined, detailing how the heating element and pressure are applied to form strong, cohesive bonds between thermoplastic composites.

The resistance welding process offers several advantages, such as the simplicity and affordability of the equipment and the ability to reprocess since the heating element remains in the composites. The biggest advantage of resistance welding is that the heat is generated exactly at the interface location.

The disassembly of thermoplastic composites is a growing area of interest, with techniques such as induction heating and resistance welding offering the potential for reducing joint strength, enabling easier disassembly. However, to the authors' knowledge, the only study on disassembly or de-welding employing resistance welding was focused on glass fiber-reinforced low-performance thermoplastics. Hence, no study in the literature focuses on the de-welding of high-performance thermoplastic composites by resistance heating. An interesting option to lower the processing temperatures is the Thermabond process, using PEI interlayer with lower processing temperature.

The end of the chapter described relevant testing procedures for fusion-bonded composites. This research uses the widely used single-lap shear experiment and the L-pull-off tests.

3

Design weld and de-weld setup

This chapter describes the design of resistance weld and de-weld experiment set-up.

A setup has been developed for the welding and de-welding of the L-pull-off specimens. Before the design of the test set-up, a functional decomposition is performed to give an overview of the tasks to fulfill. This decomposition is illustrated in Fig. 3.1 with below the (sub-)functions possible ideas and solutions:

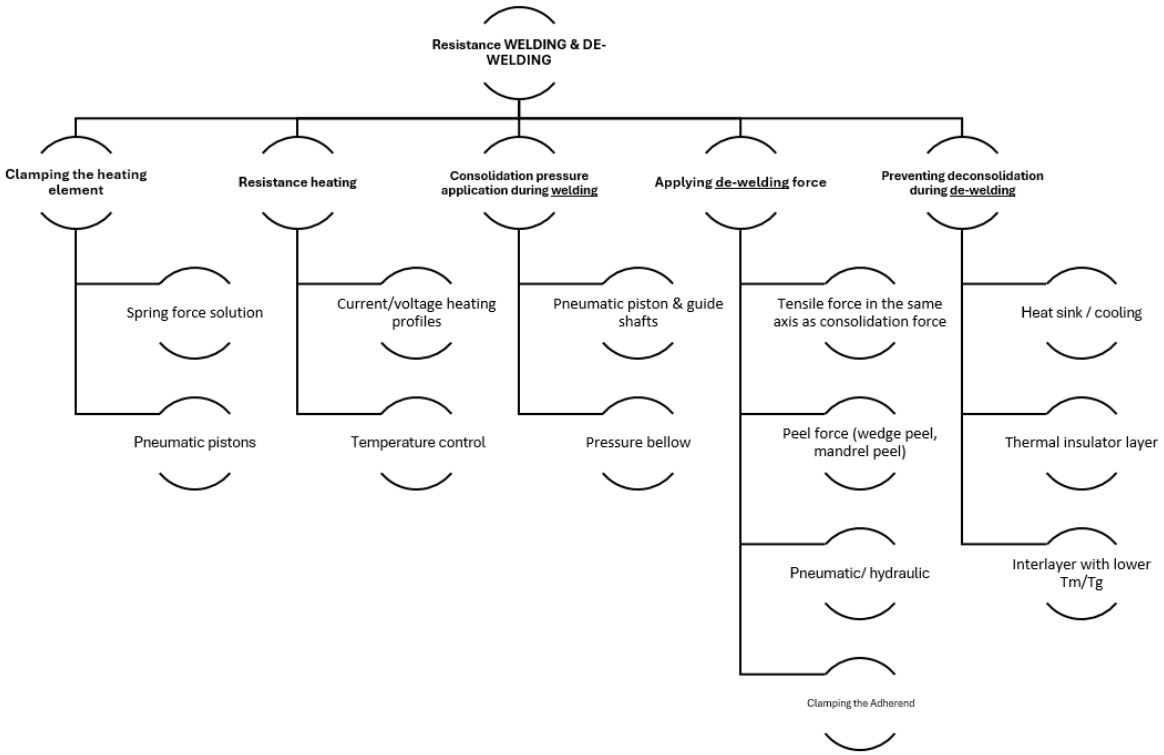

Figure 3.1: Functional decomposition resistance welding and de-welding, with possible solutions and ideas

With the functional decomposition and inspiration from different research institutes, such as DLR [8] and TUDelft [4], the resistance weld set-up with de-weld capabilities was developed. The set-up was built inside an aluminum frame shown in Figure 3.2a and consists of several parts manufactured internally at NLR.

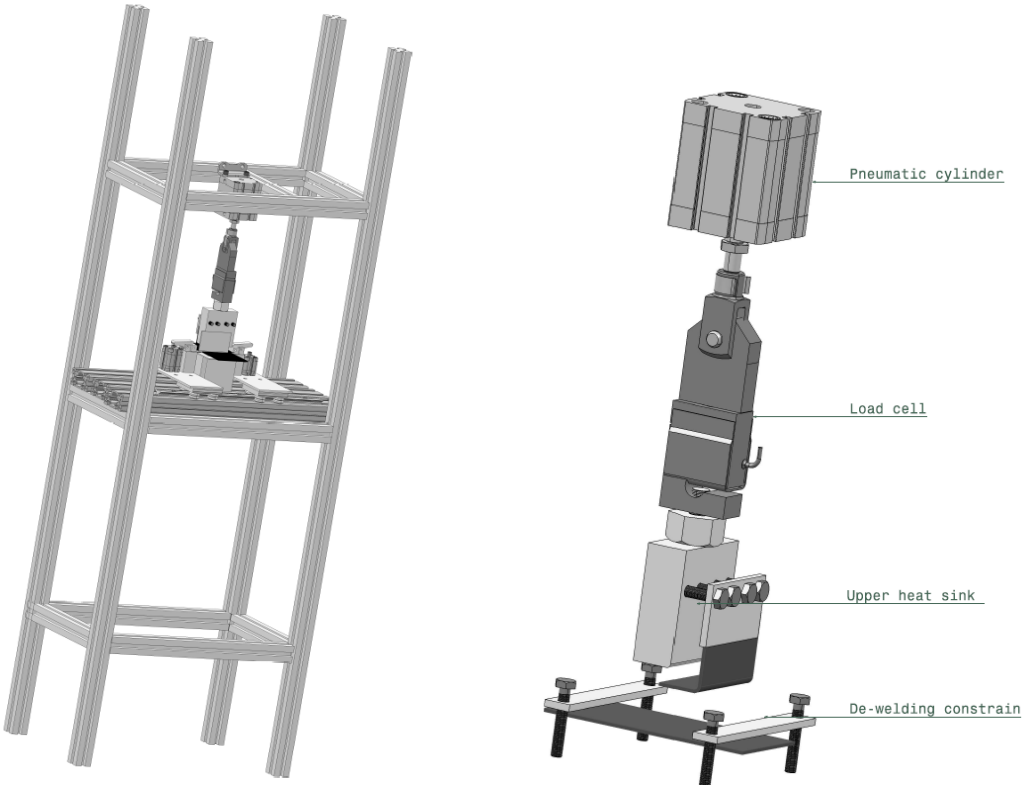

(a) Whole testbench setup

(b) Push- and press mechanism

Figure 3.2: Test setup

Force application
The pressing and pulling mechanism of the set-up is displayed in Fig.3.2b. In this mechanism, a pneumatic cylinder with a diameter of 63mm provides the weld pressure in welding and pull-off force during de-welding. The cylinder is connected to 10 bars of nitrogen, corresponding to a maximum consolidation pressure of 20 bars and a pull-off force of 3500 N. The force of the pneumatic cylinder was manually controlled using a Festo pneumatic regulator by turning the knob by hand and reading the analog pressure gauge. The speed of the piston could not be controlled.

The gripping of the L-stiffener is done based on friction; the surfaces touching the specimen were machined with roughness, and a bolt nut mechanism applied the force. The lower skin is constrained by two simple steel bars for disassembling, the spacing of the bars is 60mm, in comparison of Fig. 4.7 40mm.

Below the cylinder, a load-cell (Eurotherm SM-1000) is implemented to record the forces acting during the process. The load-cell was connected to a Eurotherm data acquisition computer to store all the measurement data. The k-type thermocouples used during welding and de-welding were also connected to this data acquisition station. The frequency of the measurements was $1Hz$.

Clamping heating element
Clamping of the heating elements is an important parameter for power input to the heating element, as identified in the literature review. Studies by Stavrov [20] and Ageorges [25] documented that a minimum clamping pressure of 1 MPa is required. Consequently, a clamping mechanism featuring a pneumatic cylinder and an aluminum arm was developed for this setup, as shown in Figure 3.3. This

setup achieves a clamping pressure of approximately 1.3 MPa, which is considered sufficient according to the literature. The blocks, made of conductive brass, have internal threads where the power source (50V 30A) is connected. The brass blocks were partly covered in electrical insulating Kapton tape, to prevent power leakage through the metal frame. Both cylinders with clamping parts, were placed on a guidance rail, initially this was done to perform weld of different sizes.

In Chapter 2, the 'edge effect' was explained as an important factor during the resistance weld process. This effect causes the edges of the joint to reach higher temperatures than other areas during the heating process. To minimize this effect, the clamping construction can be rolled against the heat sinks and minimize the air gap. Additionally, the block beneath the brass connector is made of aluminum to help cool potentially overheated spots.

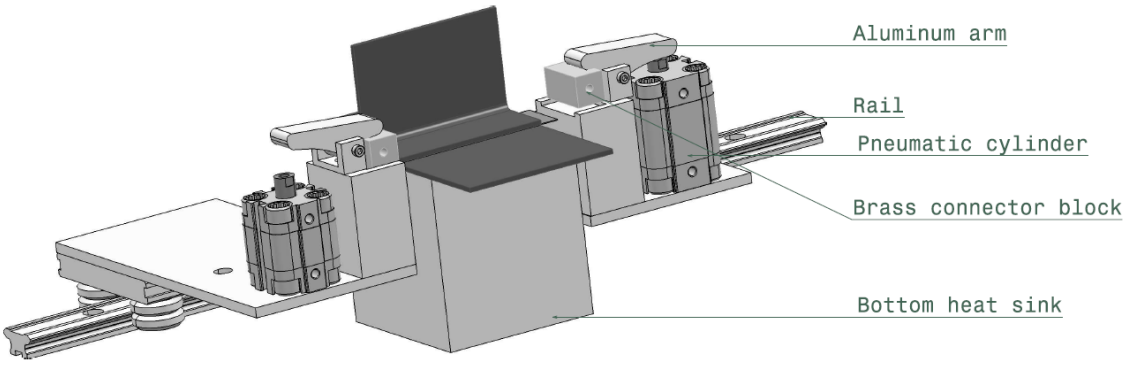

Figure 3.3: Clamping strategy

Prevention de-consolidation

The selection of the material for the heat sink is based on experiments. With these heating tests the effect of the different boundary conditions was checked. The results are shown in Fig. 3.4, with the SLS specimen in the air and at the right in between aluminum blocks. The Figure showcases an ΔT of approximately 50 $^{\circ}\mathrm{C}$ for air, and an ΔT of approximately 150 $^{\circ}\mathrm{C}$ for the aluminum BC. Note that the maximum temperature for the aluminum case is lower due to heat loss through these blocks.

With these results, the upper heat sink is designed with a volume of $204000M^3$ and the lower heat sink with a volume of $578000M^3$, the thermal conductivity is around $k_{alu} = 237W/mk$.

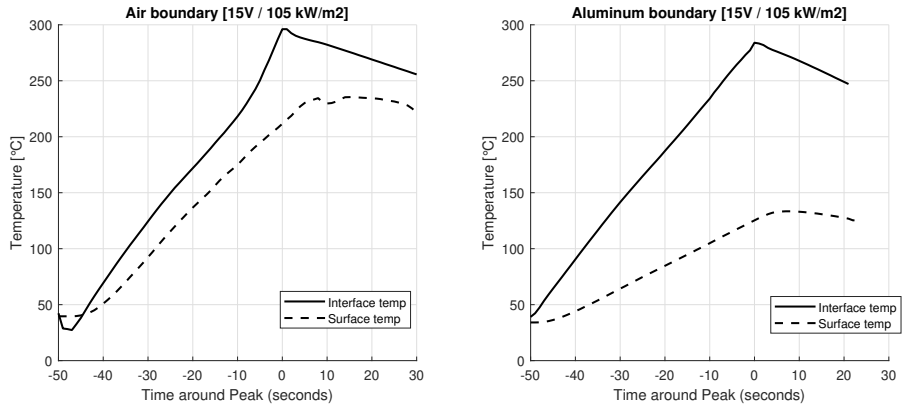

Figure 3.4: Aluminum versus air boundary condition

4

Methodology

In this chapter, the research methodology is explained. First, Section 4.1 describes the materials used for manufacturing the SLS specimens and the L-stiffener specimens. Subsequently, the manufacturing and experimental phases for both geometry types are described. The chapter concludes by outlining the modeling of the resistance heating process for prediction and validation. The results of this methodology will be described in chapter 5.

4.1. Materials

Table 4.1 provides an overview of all the materials used throughout this project, which Toray TAC® supplied. The SLS specimens used two resin types, PEI at the interface and LMPEAK for the adherends, enabling the Thermabond process described in Section 2.4). The L-pull-off specimens are composed entirely of resin-type LMPEAK, to replica a high-performance aviation assembly. A significant difference arises from using two types of glass fiber insulator layers; the PEI glass insulator layer has twice the fiber areal weight and thickness compared to the LMPEAK insulator layer, with a thickness of 0.24 mm compared to 0.12 mm.

Specimen	Name	Material
SLS	Adherends (Top & Bottom)	Carbon Fiber/LMPEAK TC1225 UD prepreg
	Interface Region	PEI TC1000
	Insulator Layer	TC1000-4HS-EC9-220g/m2
	Heating Element	TC1000-5HS-FT300B-280g/m2
	PEI Resin Film	PEI Resin Film
	Upilex Films	Upilex 25S
	Release Agent	Marbocote CE227
L Pull-Off	L Stiffener	C/LMPEAK TC1225 UD prepreg
	LMPEAK Films	LMPEAK TC1225
	Insulator Layer	TC1225-4HS-EC5-105g/m2
	Heating Element	TC1225-5HS-F300JB-286g/m2
	Skin	C/LMPEAK TC1225 UD prepreg

Table 4.1: Materials Used for SLS Coupons and L Pull-Off Specimens

4.2. Manufacturing

The de-welding of a fusion-bonded joint was tested experimentally on coupon-sized levels (SLS) and element-sized levels (L-stiffener). In preparation for the actual de-welding experiments of both types, specimens with a thermocouple embedded in the joint were produced to capture the resistance heating behaviour.

4.2.1. SLS coupons

The single lap shear test specimens were manufactured by Toray Cetex® TC1225 carbon fiber/LM-PEAK UD prepregs, laid up in a $(45, 90, -45, 0)_{2S}$ sequence, with in between an interface region made out of resin type PEI(TC1000). The stacking of the co-consolidated laminate is visualized in figure 4.1; a gap of 25.4 mm between the 0.0025mm thick upilex 25S films creates the correct consolidated joint. The upilex, a heat-resistant polyimide film, was coated three times on both sides with Marbocote CE227 release agent, to prevent bonding of the two layers outside the overlap region.

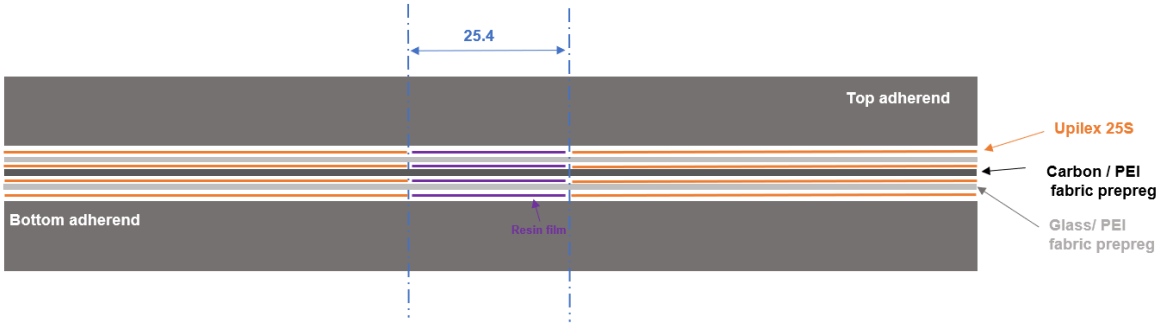

Figure 4.1: SLS coupon stacking

The bottom- and top adherends consisted of 16 layers of unidirectional tape arranged in a quasi-isotropic lay-up. The interface region consisted of a single layer of carbon fiber woven prepreg (TC1000-5HS-FT300B-280g/m2), which was used as a resistance element to heat the interface later for de-welding purposes. The glass fiber reinforced woven prepreg (TC1000-4HS-EC9-220g/m2) was used as an electrical and thermal insulator between the heating element and the adherends. As Toray does not offer a PEI matrix glass scrim, a thicker insulator layer was used. An added layer of PEI resin film was placed on either side of the interface to improve bonding between the substrate and insulator layer. All constituents were consolidated following the autoclave program in Figure 4.2. Metal blocks covered in Marbocote coated upilex were placed around the edges of the laminate to prevent any resin from flowing out, and a steel plate on top of the laminate to create a flat surface.

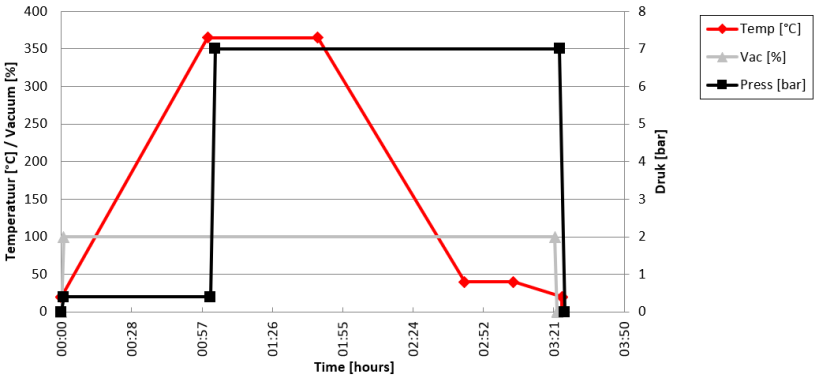

Figure 4.2: Autoclave cycle

After consolidation in the autoclave, the laminates were cut in the dimensions of the standardized SLS specimen. First, the excess unbonded parts of the plates were cut away from the joint using a cutting and grinding machine (figure 4.3a). Subsequently, the consolidated plate was cut into 25,4 wide strips, see figure 4.3 b. The SLS specimens for dewelding got an extra tab connected for alignment in mechanical tests. The SLS specimens for heating tests got a thermocouple embedded at the interface. The 0.1 mm thermocouples were manually assembled in the lab. The process began by stripping the insulation from the thermocouple wires and twisting the exposed ends together. Finally, the twisted wire ends were welded using a spot welder and covered in Kapton tape for electrical insulation.

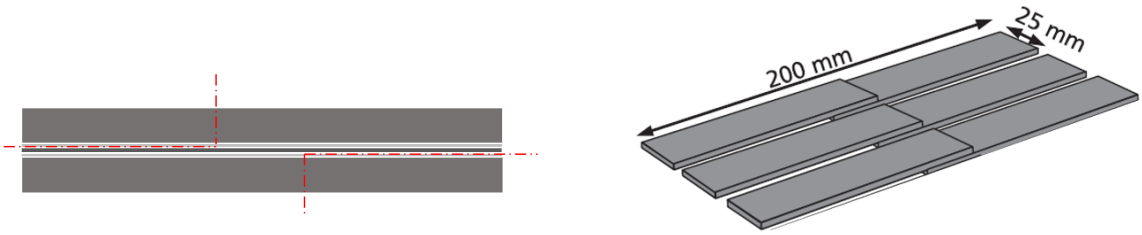

Figure 4.3: Cutting of the consolidated plate to the right SLS dimensions

4.2.2. L-pull-off

The second test configuration was the L-pull-off. Several manufacturing steps had to be taken to prepare for the de-welding of these specimens. First, all the materials in preparation for welding L stiffener onto the flat skin by resistance welding had to be obtained. These materials, collectively called a weld stack, are illustrated in Fig. 4.4a and detailed in Table 4.2.

The resin type for all materials was Toray's LMPEAK resin. The dimensions, shown in Fig. 4.4b, are based on a common stiffener spacing of 150–160 mm in aircraft structures, as stated by Kassapoglou[9]. Internally at NLR, these dimensions were also used for induction welded samples.

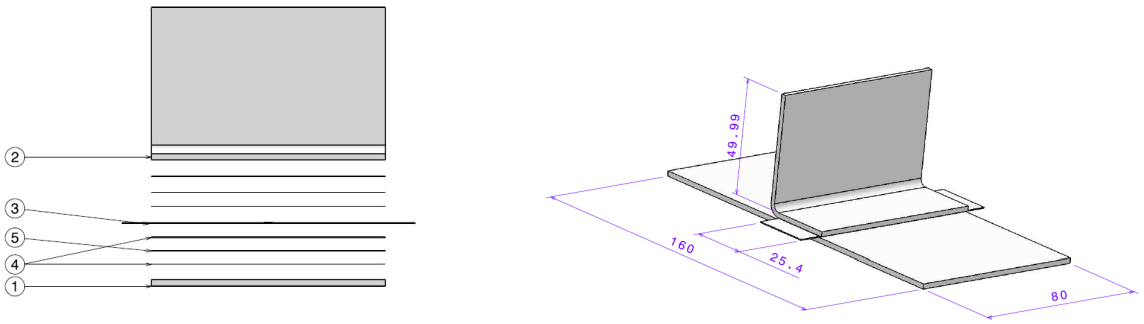

(a) Weld stack

(b) Dimensions, in mm, L-pull off specimen

Figure 4.4: Specification L-pull-off specimen

Table 4.2: Materials for one L-pull-off specimen

Number	Name	Material	Quantity	Thickness (mm)
1	L stiffener	C/LMPEAK	1	2.3
2	LMPEAK films	LMPEAK	4	0.01
3	Insulator layer	G/LMPEAK 105 gsm fabric tape	2	0.12
4	Heating element	C/LMPEAK 286 gsm heating element	1	0.3
5	Skin	C/LMPEAK	1	2.3

The L stiffener and flat skin were made of Toray Cetex® TC1225 UD prepregs, and hand-laid in a quasi-isotropic (45,90,-45,0)2S order. The laminate, 650 x 650 mm, was then consolidated in the autoclave by the program shown in Figure 4.2. A piece of this laminate was used to obtain the flat skin by cutting it to the right dimensions(80*160mm) with a saw. From the other piece the L-stiffeners were obtained, by first cutting it to plates with a dimension of 500x160mm. These plates were then stamped formed into an L-shaped stiffener by first putting them in an infrared oven and, heating it up to 385°C, and quickly pressing it into a mold with a Wickert pressing machine. The last step was to cut these L-shaped plates into the right dimensions: height 50mm, base 30mm, and width 80mm.

The LMPEAK films provide a resin-rich region within the weld area, improving the intimate contact [45]. These films were cut from a roll, and ultrasonic spot welded on the heating element to secure a good placement.

The insulator layer is a 105 gsm e-glass woven fabric tape, preventing the current from flowing through the laminates. The layer was cut and consolidated prior in an autoclave by the same program shown in Figure 4.2.

For the heating element a woven carbon fiber, H5 satin weave, prepeg layer was used. (based on literature from [37, 22]) The fabric (286 gsm) was used to introduce the current in the carbon fibre bundles, the LMPEAK matrix was burned away from both ends of the element over a length of 10 mm using a ultrasonic welding device. Figure 4.4b shows this as the sticking-out areas.

The last step in manufacturing the L-pull-off specimens was consolidating all materials into a L-pull-off specimen by resistance welding. The process parameters are based on a study from DLR [37]; from this study, four stages are drawn, listed below in table 4.3. The pressure of 8 bar represents a force of 2000 N, which was controlled by the load cell.

The voltage and duration depend on the specific resistance of the specimen, but they were generally be around these values. The specimens welded without thermocouple were controlled by monitoring the force measurements. When applying a constant force, a typical load variation for semi-crystalline thermoplastics is noted by [20] and [22]. The load decreases sharply while melting and flowing starts in the welding process; this is the moment to apply the 8 bars of pressure and turn off the power source.

Table 4.3: Weld processing stages

Stage	Name	Duration	Voltage	Pressure	Interface Temp
1	Heating	90-120 sec	25 V	1 bar	-
2	Melting	10 sec	27 V	8 bar	$T_{\text{process}} = 340 - 360$°C
3	Crystallisation	25 sec	18 V	8 bar	$T_{\text{crystalline}} = 215 - 235$°C
4	Cooling	30 sec	0 V	8 bar	-

4.3. Experiments

De-welding experiments were performed on two types of geometries: SLS coupons and L-pull-off specimens. The SLS coupons were based on a quantitatively standard test procedure used for disassembly, while the L-pull-off de-welding was more qualitatively tested in the developed test bench.

4.3.1. Experiments SLS-coupons

Heating tests These experiments aimed to obtain various heating profiles and examine the through-the-thickness heating behavior, particularly focusing on how different voltages influence the heating profile. Additionally, the experiments explored the impact of boundary conditions, comparing air (an insulator) with aluminum (a heat sink).

The SLS specimens were tested using the setup illustrated in Fig. 4.5. A thermocouple was embedded at the center of each specimen before consolidation in the autoclave, while another thermocouple was taped to the bottom surface with Kapton. An infrared camera was used to monitor and validate the surface thermocouple readings. A total of 15 specimens, each containing an internal thermocouple, were subjected to various currents. The interface and surface temperatures were measured using both thermal imaging and thermocouples. In total, 47 heating experiments were conducted with this setup.

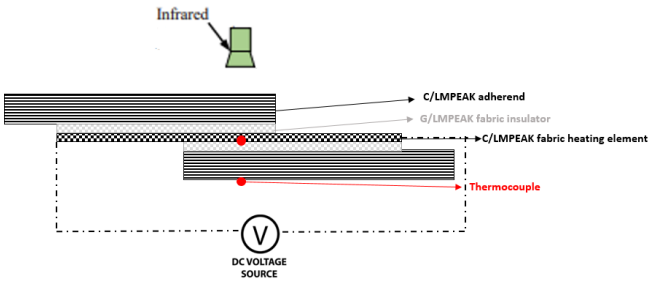

Figure 4.5: SLS heating experiment setup

De-welding Figure 4.6 shows the test setup for SLS de-welding. An Instron 100 kN test bench universal testing machine was used. The current source was attached to the resistance element through copper clamps. These were placed as close to the interface as possible to avoid heating the carbon fabric outside the overlap region. Before clamping, the fabric heating element had to be stripped of resin with an ultrasonic welding device to ensure good conduction. A FLIR A70 thermal imaging camera was used to record the surface temperature of the samples during heating. The temperature was measured and averaged for a circular region in the center of the interface. Test specimens were heated manually by adjusting the current. After reaching the target surface temperature, shear loading was applied until failure.

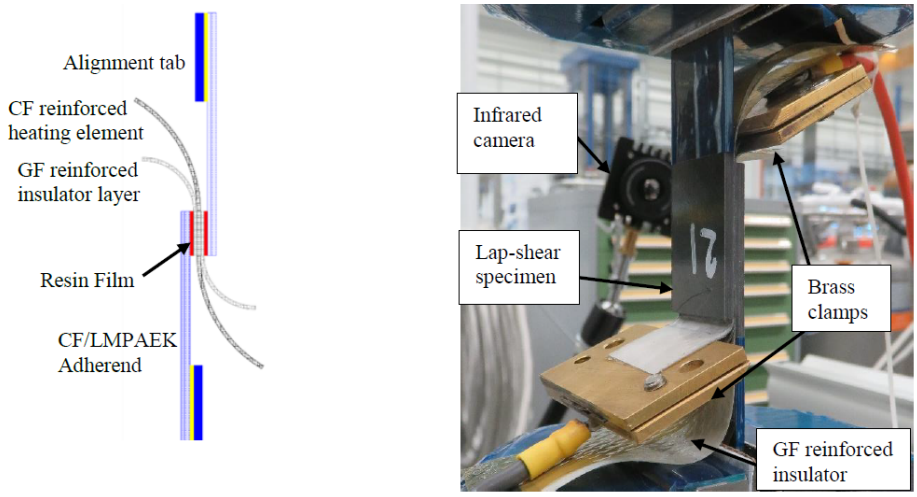

Figure 4.6: SLS de-welding experiment setup

PEI is known to weaken substantially above its T_g of 217°C [46]. The de-weld temperatures were chosen around this glass temperature; the test temperature range was set to 190 - 290 °C. In table 4.4 the seven tested interface temperatures are listed. These temperatures were obtained by extrapolating the interface temperature to the outer surface temperature with the information from the heating experiments. For each temperature, a minimum of three specimens were tested. Three samples tested at room temperature served as a reference.

Table 4.4: De-welding Test Temperatures for PEI Interfaces

Material	Test Temperatures
PEI	RT, 190°C, 225°C, 240°C, 250°C, 260°C, 280°C,

4.3.2. L-pull-off experiments

The de-welding experiments of the L-stiffeners were performed in two batches, one of 12 specimens and one of 6 specimens. The specimens were tested in the developed test-bench, previously described

in chapter 3. Table 4.5 lists the L-pull-off specimens with their corresponding de-weld temperature. For both batches, the de-welding was performed at room temperature for reference testing and above the melt temperature of LMPEAK (315°C). In the first batch, the de-welding temperature of 245 °C was added to test the de-welding at lower temperatures (faster and lower energy consumption). The fracture surface of the de-welded specimens was visually observed.

Table 4.5: Test Series Information

Test series-ID	TC	Interface Temp [°C]	Surface Temp [°C]	Remarks
Lpull-DW-LMPEAK-(1-4)	Yes	345 ± 10	Measuring	Above T_m
Lpull-DW-LMPEAK-(5-10)	Yes	245 ± 10	Measuring	Find basevalue
Lpull-DW-LMPEAK-(11-12)	Yes	RT	RT	Reference tests
Lpull-DW-LMPEAK-(13-14)	No	RT	RT	Reference test
Lpull-DW-LMPEAK-(15-18)	No	345 ± 10		Above T_m

Specimens 11, 12, 13, and 14 are tested by following the airbus standard [47] to determine the baseline weld strength and were not tested in the resistance de-weld setup. The load reaction is ensured by two metallic roller bars symmetrically positioned; see below in Fig. 4.7. The test fixture must ensure the symmetric positioning of the L-profile during the test. The specimens are loaded with a constant cross-head displacement of 1 mm/min until failure, using an Instron 100 kN testing machine.

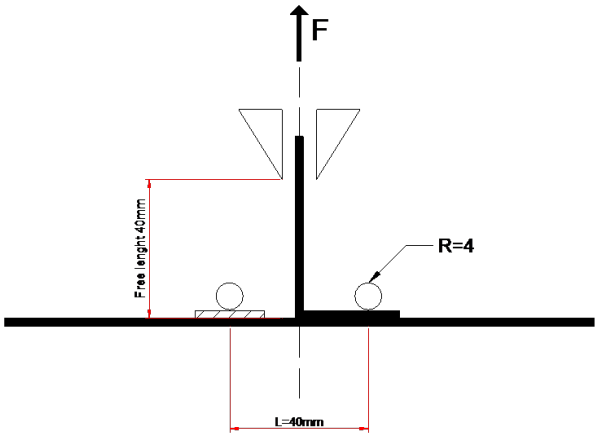

Figure 4.7: Schematic test set-up stiffener L-pull-off testing (dimension in mm). - Airbus standard RE1801807

4.4. Numerical heat model

Together with the experiments, the resistance heating process was modeled using Abaqus®. With these simulations, a better idea of the process parameters required to heat the samples to the necessary temperatures was gained. After validation, the model could also be useful in investigating the different (boundary) materials and dimensions. The first part of this section describes the underlying theory. Then, the joules heating and the material properties are modeled, and joules heating physics are inserted. The model is completed by applying a mesh of finite elements.

The model is a basic three-dimensional transient finite element model, orthotropic heat conduction. The welding pressure was not included in the model as it was assumed that during welding and de-welding sufficient contact was achieved, which minimize the effect of the variable. The more assumptions were carried:

- Perfect consolidation
- Laminate is modeled as one material block, stacking neglected
- Power loss due to contact resistance are neglected

4.4.1. Theoretical background

The heat conduction in the material is governed by the 3D transient heat equation, which accounts for temperature-dependent thermal properties and the generation of heat due to Joule heating;

$$\frac{\partial}{\partial x}\left(k(T)\frac{\partial T}{\partial x}\right)+\frac{\partial}{\partial y}\left(k(T)\frac{\partial T}{\partial y}\right)+\frac{\partial}{\partial z}\left(k(T)\frac{\partial T}{\partial z}\right)+Q=\rho c_p\frac{\partial T}{\partial t} \tag{4.1}$$

where ρ is density, c_p is heat capacity, T is temperature, t is welding time, Q is the heat generation and k is thermal conductivity. Once the heat generation is known as a function of time with all the material properties, the 3D transient heat problem can be solved.

The boundary condition to all free boundaries was set as free convection, surface-ambient radiation was not considered, resulting in the following equation:

$$-k(T)\frac{\partial T}{\partial n}=h(T-T_\infty) \tag{4.2}$$

where $\mathbf{n}$ is the normal vector of the boundary, h is the free convection coefficient to air ($h=9\,\mathrm{W/m^2K}$), and T_∞ is the ambient temperature.

The equation is then solved using numerical methods due to the complexity introduced by the non-linearity in thermal conductivity $\kappa(T)$, complex geometry, and the time dependency. Therefore, the model domain is discretized into small elements (FEM) using Abaqus® software, and the temperature field is approximated within each element. The implicit method was selected, where for every step equilibrium is enforced with a Newton-Raphson algorithm.

4.4.2. Material properties

In this model, temperature in- and dependent properties are used. The composite layers consist of Toray Cetex® TC1225 LMPAEK/TC1225 prepegs, woven and UD plies.

The carbon fiber laminates with a $(45, 90, -45, 0)_{2S}$layup was considered an orthotropic material, with three perpendicular conductivities k_x, k_x and k_z. The values for these properties were provided by Toray and are confidential; these are temperature-dependent. These ply-properties were used as laminate properties.

The glass fiber insulator layer was considered isotropic because it is a very thin layer where the conductivity in the z-direction is most important. The conductivity of the glass fiber layer is listed in table 4.6, and this value is checked with the rule of mixtures formula. With the known fiber volume fraction and the conductivities of the constituents, the conductivity through the thickness of the glass fiber/LM

peak at room temperature is [21]:

$$k_z = \frac{k_{\text{matrix}} k_{\text{glass}}}{k_m v_f + k_{\text{glass}} v_m} = 0.42 W/mK \tag{4.3}$$

Where k_{glass} is the thermal conductivity of glass fiber, computed with the properties of E-glass fiber of supplier AGY®. k_m is the thermal conductivity of the LMPEAK matrix, calculated with the PEEK values [28]. v_f and v_m are the fiber and matrix volume fractions, respectively. The result is close to the value in table 4.6.

Table 4.6: Temperature independent properties for the simulations

Property	Symbol	Value	Reference
Insulator density	ρ	$1530\,\mathrm{kg/m^3}$	Toray Cetex® TC1225: Product data sheet
Laminate density	ρ	$1590\,\mathrm{kg/m^3}$	Toray Cetex® TC1225: Product data sheet
Aluminum density	ρ	$2710\,\mathrm{kg/m^3}$	[48]
Insulator thermal conductivity	$k_{insulator}$	$0.38\,\mathrm{W/(m\cdot °C)}$	C.Ageorges [21]
Aluminum thermal conductivity	k_{alu}	$237\,\mathrm{W/(m\cdot °C)}$	Jitha S. Jayan et al[48]
Aluminum specific heat	Cp_{alu}	$900\,\mathrm{J/(kg\cdot °C)}$	Jitha S. Jayan et al [48]
Air convection coefficient	h	$9\,\mathrm{W/(m^2\cdot °C)}$	T. Koenis [49]

Specific heat capacity
In the study of Farkas [50], the temperature-dependent specific heat capacity of a CF/PEEK composite was measured. These values were implemented in the model to represent the CF/LMPEAK composite. For the temperature-dependent specific heat capacity of the G/LMPEAK layer, the obtained values by Lineotta et al. [51] the rules of mixture were picked.

Table 4.7: Temperature-Dependent material properties; Specific Heats of the carbon fiber composite

Temp ($^\circ$C)	Glass Fiber/PEEK	Carbon Fiber/PEEK
	Specific Heat C_p ($\mathrm{J/(kg\cdot °C)}$)	Specific Heat C_p ($\mathrm{J/(kg\cdot °C)}$)
20	850	750
50	1000	900
100	1250	1050
150	1450	1100
200	1600	1300
250	1800	1610
300	2100	1800
325	2300	2050

4.4.3. Power input

Joule heating is implemented in the simulations as a volumetric heat flux using a DFLUX subroutine in Abaqus. The volumetric heat input is calculated according to Equation 4.4. This calculation neglects power losses due to imperfect electrical connections between the heating element and the clamps. It is assumed that the power passing through the heating element is equivalent to the power supplied by the electrical source:

$$q''' = \frac{UI}{wtl} = \frac{U^2/R}{wtl} = \quad W/m^3 \tag{4.4}$$

With the electrical parameters, where U the voltage across the heating element, measured in volts $[V]$, R the electrical resistance of the heating element, measured in ohm's $[\Omega]$. And the physical parameters: the width w, thickness$[t]$ and length l of the heating element in meters $[m]$.

The resistance of a woven carbon fiber heating element depends on temperature; it decreases as temperature increases [16, 12]. Consequently, applying a constant voltage results in an increasing

volumetric heat generation $[q''']$, as illustrated by the second part of Eq. 4.4. To incorporate this behaviour into the model, the voltages and currents of the heating element were monitored during the heating processes. Using Ohm's law, the temperature-dependent changes in resistance were then determined.

The temperature depended resistance of the woven heating element (25*110mm) is plotted in Figure 4.8a. The reduction of the resistance is approximately 18% at 340°C, the bars show the measured bandwith. In contrast, Ageorges [25] noted a linear decrease of 10% at 340°C for a woven C/PEEK heating element (25*160mm). DLR's study reported a reduction of 10% for the same material but a longer heating element (25*260mm).

The consequence of this phenomenon is that power input (W/m^2) is not constant; the lower resistance will result in more heat generation when applying a constant voltage. In Fig. 4.8b, such a typical rise in power density caused by the reduction in resistance is shown over time.

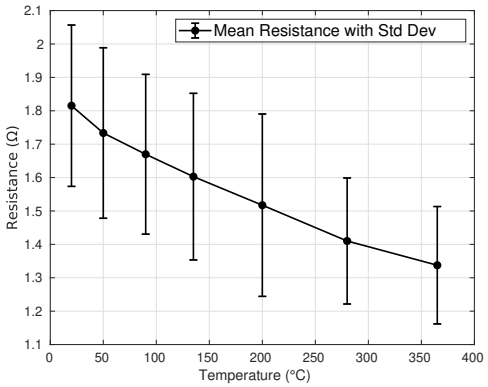

(a) Reduction of resistance up to processing temp of 365°C.

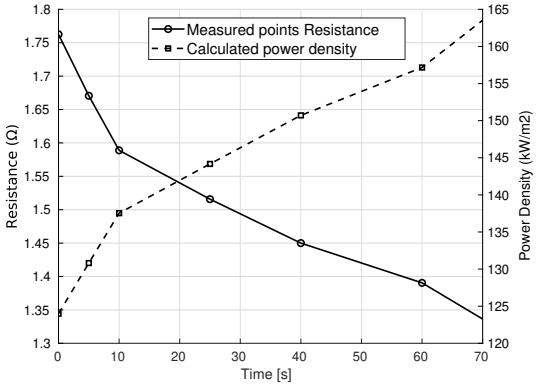

(b) Typical behaviour of resistance and power over time, for a 25V case t = 70 sec

Figure 4.8: Resistance characteristics of a H5 satin weave heating element (286 gsm)

So, the volumetric power input could be calculated with a decrease in resistance. Below in table 4.8, these values for a 25V constant voltage case are presented.

Voltage [V]	Resistance [Ω]	Power [W]	Volumetric Power Density [W/m³]
25	1.56	400	4.0×10^8
25	1.43	437.5	4.37×10^8
25	1.36	462.5	4.62×10^8
25	1.32	475	4.75×10^8
25	1.25	500	5.0×10^8
25	1.22	512.5	5.12×10^8

Table 4.8: Calculated volumetric power input values, for a constant voltage of 25V as the resistance decreases with increasing temperature

4.4.4. Geometry and mesh

Regarding finite element analysis, the model illustrated in Figure 4.9 was discretized using eight-noded brick elements with heat transfer properties. The analysis was conducted with the ABAQUS V5.5 finite element software. The convergence of the finite element model was assessed to determine the sensitivity of the solutions to mesh refinement. The number of elements along the x- and y-axes remained unchanged (see Figure 4.9), while the elements along the z-axis (thickness) were refined to capture the heat flux through thickness. Especially around the heat element, the mesh was refined, and further away, coarse mesh was used to provide numerical solutions with an acceptable accuracy/computing time combination. In total, 13845 solid hexahedral elements were used in the simulation.

At the start of the simulation, all domains were set to room temperature (20°C).

The volumetric heating load was mapped to the mesh of the laminate, which is red visualized in Fig. 4.10.

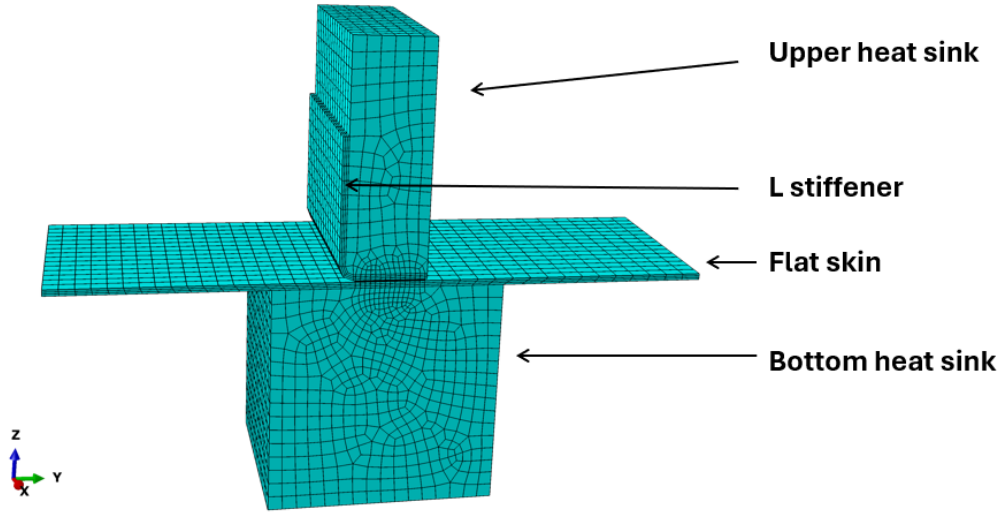

Figure 4.9: 3D model with mesh visualized, local refinement around heating element in Z-direcion.

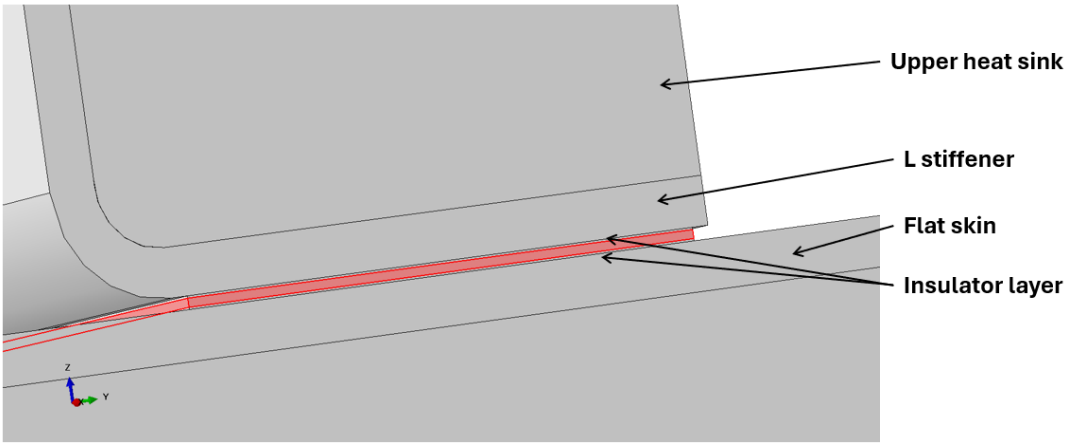

Figure 4.10: Zoom in with heating element visualized in red

5

Results

In this chapter, the validation and results of the model will be addressed first. Then the heating behaviour results of the de-welding experiments of the SLS are presented, followed by those of the L-pull-off specimens.

5.1. Model validation

In this section, the validity of the model is assessed by measuring the heating behaviour of the L-pull-off specimens. The heating data was collected by performing heating tests with K-type thermocouples. The measured data also analyzed the heating profile through the thickness. At last, the sensitivity of the model to changes in material properties was evaluated.

The graphs in Figure 5.1a and 5.1b illustrate the comparison between the measured and modeled temperature profiles for 20V and 25V cases. Although there is a good agreement between the simulated maximum temperature and the actual measurements, the model predicts a significantly faster temperature rise. This influence is more apparent by the lower power input, the 20V case.

The modeled temperatures drop off rapidly, whereas the measured temperature decreases more gradually. This suggests that the model predicts a faster cooling process than observed in the experiments. Also, the temperature rises faster than measured and levels off. This discrepancy likely arises from the assumptions of perfect contact and power generation in the heating element. The model presumes that the contact between the laminates and heat sinks is perfect, resulting in direct heat conduction within these components. This is only true when perfect intimate contact is achieved [21]. For the power generation, it is assumed that the power supplied is transferred entirely to the heating element, as described by Eq. 2.2 in section 4.4.3, without accounting for power losses in the wires, clamps, and the contact points between the fiber bundles and the clamps.

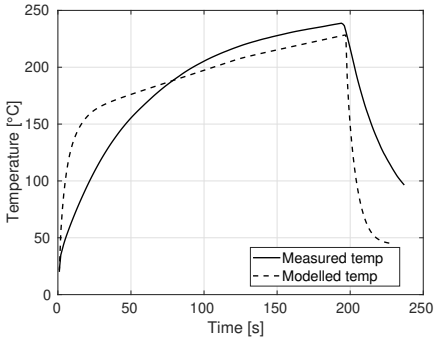

(a) Comparison between measured and simulated temperature histories for constant 20V

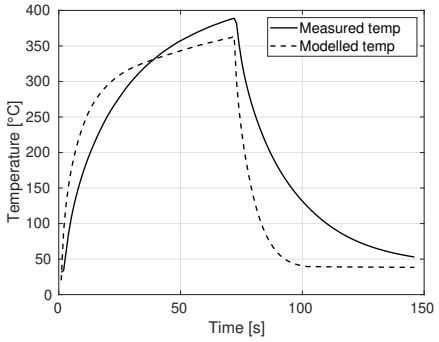

(b) Comparison between measured and simulated temperature histories for constant 25V

Figure 5.1: Comparison between measured and simulated temperature histories

Through Thickness

The heating profile through the thickness is an important aspect of the de-welding process. In Fig. 5.9, the modeled and measured surface temperature of Fig. 5.1b is shown. Fig. 5.2 shows the temperature curve for the surface of the L-stiffener under the constant 25V condition. This Figure graphically illustrates the measured and modeled surface temperatures, highlighting a difference in peak temperatures of 4°C.

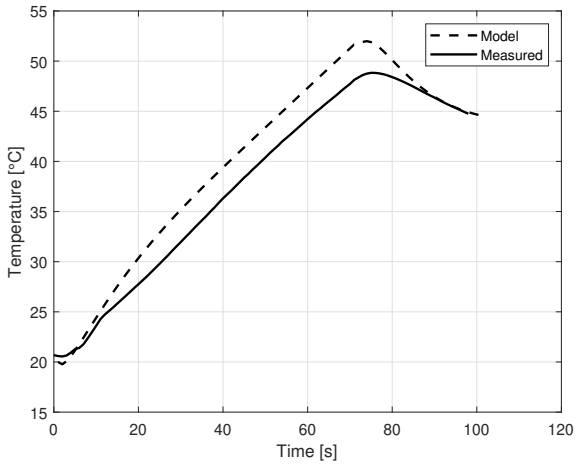

Figure 5.2: Surface temperature, measured and modeled, for a constant 25V. The corresponding interface temperatures shown in Fig. 5.1b

Also, a sensitivity analysis was performed. This analysis considered the critical material parameters in the model. Each parameter was increased by 10%, after which the temperature at the location was compared to the baseline value (280 $^{\circ}\mathrm{C}$), after a simulation time of 60 seconds. The relative differences are graphically represented in Fig. 5.3. Clearly, the input q''', the specific heat capacity of the laminate C_p, and the density of the laminate ρ, have a powerful effect on the temperature.

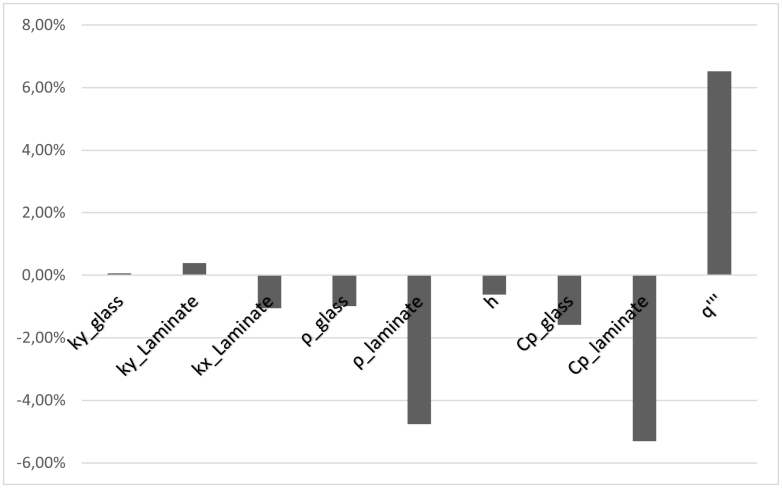

Figure 5.3: Effect of 10% increase on the temperature

5.2. SLS de-welding

This section gives the results of the de-welding experiments. Before the de-welding experiments, heating tests were carried out to determine the process conditions; this is first described in the section on heating behaviour.

5.2.1. Heating behaviour

The SLS specimens were tested within an interface temperature range of 190 to 270 degrees Celsius. This range was chosen because the strength of PEI rapidly decreases after reaching its glass transition temperature,$T_{glass} = 217°\mathrm{C}$. During the de-welding experiments, the interface temperature was controlled by the surface temperature; these surface temperatures were determined by performing a heating test on SLS specimens with thermocouples embedded. Initially, the heating tests were conducted in the transient region to speed up the de-welding process and minimize the effect of heating the adherend. The influence of speed on the surface temperature is displayed in Fig. 5.4a; in both cases, interface temperature of 250 $°\mathrm{C}$was objected to; the black line represents a heat rate approximately three times faster than the grey line. The first heating cycle shows a temperature difference, $\Delta T = T_{interface} - T_{surface}$, of 100 degrees Celsius. The second heating cycle (grey line) displays a temperature difference of 40 degrees Celsius. However, as the speed increases, the temperature lag at the surface boundary also relatively increases, making it harder to control with the surface temperature. With this phenomenon, it was chosen to simplify the experiment to steady-state situations. The consistency of the experiments could be more guaranteed; nevertheless, affecting the adherend becomes more of an issue, as shown, and more energy is required.

The second heating test was performed to relate the interface-surface temperatures under steady-state conditions. The heating tests and later de-weld experiments were simplified to a heating cycle, as shown in Fig. 5.4b. The Figure displays three distinct phases: heating, adjusting, and steady-state. In the first phase, the specimen was heated up to the de-welding region, and then the temperature was manually adjusted to reach a specific surface temperature; in the last phase, the correct power supply was found, and steady-state conditions were reached, the disassembling can start.

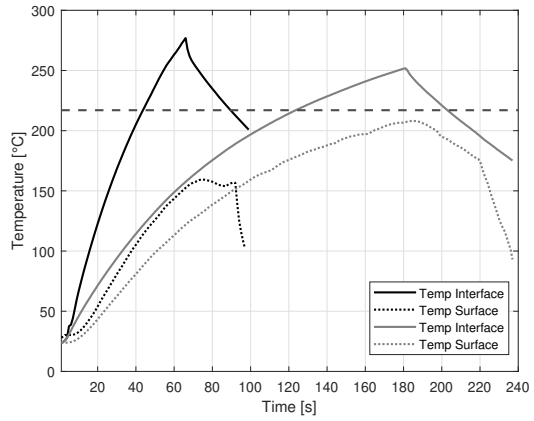

(a) Comparison between measured temperature histories for; black line 12V and 60 seconds and grey line 180 second 10V

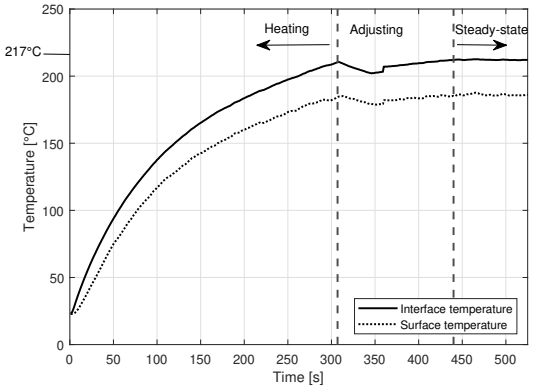

(b) De-welding strategy, heating phase with constant voltage of 7V, adjusting phase in this to go to 215°C interface temp, steady state region with interface Temp 215°C and surface temp 185 °C

Figure 5.4: Heating characteristics SLS specimens

Interface - surface temperature correlation

Before performing the de-welding experiments, the objective interface temperature had to be projected to the surface temperature to control the experiments. This temperature difference (Δ T °C) is numerically calculated by doing steady-state simulations in the model and measured by heating experiments. The heating experiments were performed by doing the cycle illustrated in Fig. 5.4b for various temperatures listed in Table 5.1.

The model was simplified to a 2D SLS geometry, extended with emissivity ϵ of 0.9 for the laminates based on the value used by Grouve [52]. The steady-state simulations are elaborated in the appendix.

Fig. 5.5 displays the results of this simulation; here, the through-thickness temperature distribution is plotted for an interface temperature of $T = 235°\mathrm{C}$.

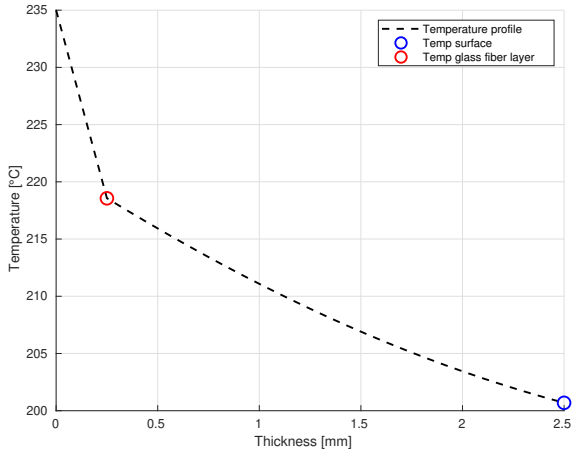

Figure 5.5: Through thickness illustration numerical - steady state 235°C interface temperature

The results of the simulations are summarized in table 5.1 with the corresponding surface interface temperatures. The table shows that the model overestimated the measured surface temperatures. During these simulations it was noted that the air convection value was of high influence and could be more detailed incorporating the exact geometry and temperature-dependency.

Interface temp (°C)	**Surface temp (°C)**	
	Measured	**Abaqus**
190	-	171
210	170	181
235	200	202
260	220	223
290	238	246

Table 5.1: Comparison of surface temperatures for different interface temperatures using Measured and Abaqus data.

5.2.2. Results SLS de-welding experiments

Table 5.2 shows the test results of the SLS de-welding experiments. The table summarizes the results of these experiments, including the number of experiments conducted at each temperature, the mean shear strength, and the standard deviation. The remaining strength of the specimens was calculated using the maximum load and the weld area (25.4 x 25.4mm).

Surface Temp (°C)	**Interface Temp (°C)**	**Experiments**	**Mean shear Strength (MPa)**	**Standard Dev.**
25	25.00	4	23.02	0.60
150	189.44	3	17.44	0.27
175	225.28	3	7.04	0.71
187	240.64	3	3.60	1.00
195	247.04	2	2.18	0.36
200	254.24	3	1.20	0.30
211	267.52	3	0.58	0.10

Table 5.2: De-welding results. Interface temperatures are computed with help of the model and fracture behaviour analysis.

Figure 5.6, graphically presents the results in table 5.2 in a strength versus temperature Figure. The

surface temperatures represent measured values while the interface temperatures are estimates obtained from the interface-surface correlation in section 5.2.1. The curve linking the data points is based on linking the transition points in the de-welding behaviour to the glass transition temperature of the polymer. The graph illustrates that the material's lap-shear strength reduces as temperature increases.

At room temperature (25 $^{\circ}$C), the mean shear strength was 23.02 MPa, with a standard deviation of 0.60 MPa, across four experiments. At the initial testing temperature of 190°C, well below the Tg of PEI, a drop-off of 24% in SLS strength occurs already. Exceeding Tg, the SLS strength decreases rapidly but levels out later, retaining some strength up to 270°C. This behaviour is typical for amorphous polymers, which soften rapidly when surpassing their glass-transition temperature [13, 16].

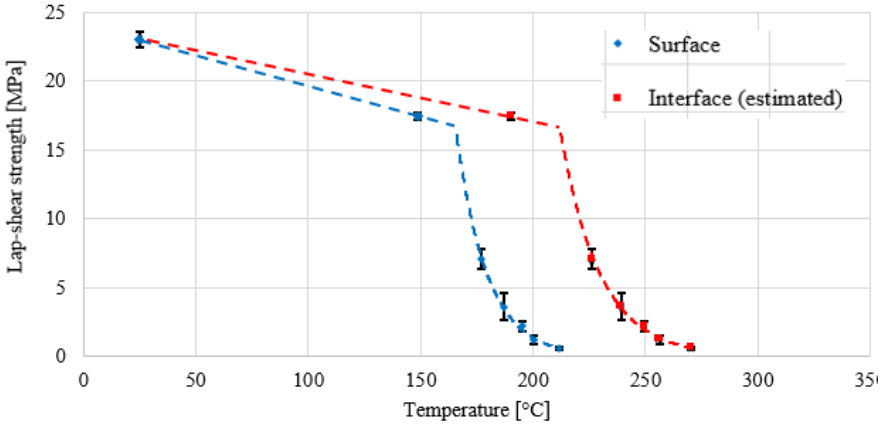

Figure 5.6: Strength versus temperature curve of the SLS specimens, blue surface data points are measured with standard dev. Interface temperatures are calculated

5.2.3. Fracture behaviour

The fracture surfaces of the SLS specimens at the tested interface temperatures are shown in Fig. 5.7. At room temperature (23 $^{\circ}$C), failure is primarily observed in the adherend. At the initial testing temperature of 190°C, well below the Tg of PEI, fracture at this point occurs in the heating element. As the temperature surpasses T_g at 225 $^{\circ}$C, the shift towards matrix-dominated specimen separation happens, and good de-welds were achieved. This is a consistent pattern across all tested temperatures beyond this point. This rapid softening behavior beyond the glass-transition temperature is characteristic of amorphous polymers. PEI interfaces continuously separated in the matrix-rich region between the insulator and the adherend. This is likely to result from the interface between the two polymers representing a weak point.

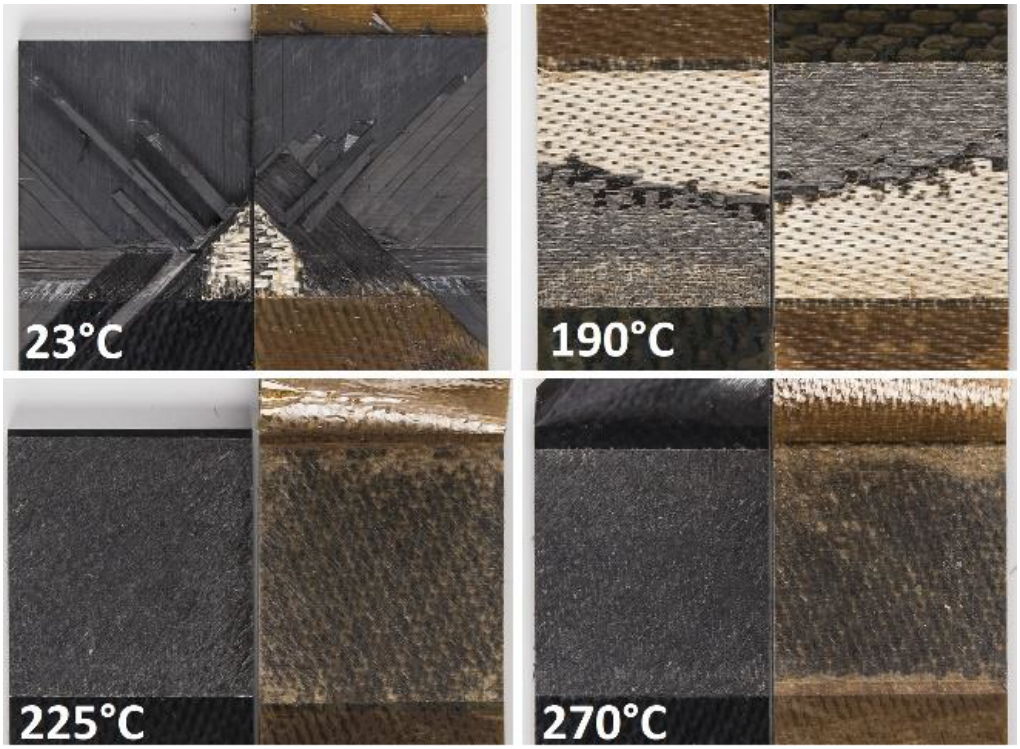

Figure 5.7: Fracture surface of SLS coupons after de-welding at various interface temperatures.

5.3. L stiffener de-welding

The results of the dewelding of the l stiffeners will be described by first explaining the heat characteristics, the failure at room temperature, and the dewelding results with fractual behaviour (divided into two batches). A total of 18 L pull-off specimens were tested (see table 4.5) using the developed test bench.

5.3.1. Thermal behaviour

This section discusses the thermal behaviour of the L-pull-off specimens. The results presented in this section help choose a strategy for the de-welding experiments and support the discussion of the specimens' failure mechanisms.

The temperature versus time curves for four constant voltages are depicted in Fig. 5.8. The heating behavior was measured at the core of the specimen, with the positioning indicated in Fig. 5.8. The curves for 20V and 15V did not reach the melting temperature of LMPEAK within the given timeframe, suggesting that an applied voltage above 20V is necessary for effective de-welding. The 30V curve reaches the melt region within 20 seconds, whereas the 25V curve reaches that within 40 seconds.

According to the findings of studies [20, 25], the temperature at thermocouple location 1 is the lowest in the middle axis of the weld. This baseline ensures that the entire interface exceeds the melting temperature when following this 25V curve for up to 40 seconds. A constant power input of 25 volts was chosen for the de-welding experiments because, with this heating rate, the test bench could be controlled manually individually. So, under these conditions, heating takes 40 seconds, after which the force can be applied. The power density under these conditions was around 170 $kW/m2$.

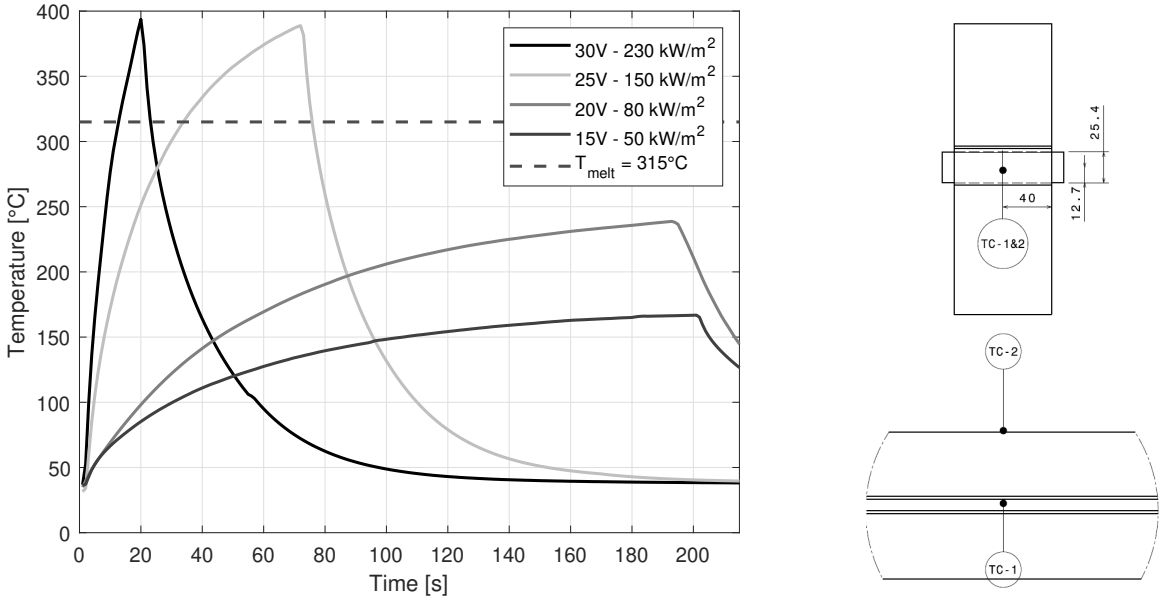

Figure 5.8: Left; measured heating curves for constant voltages, average power density given per voltage the legend. Right; positioning of the thermocouples, Thermocouple 1 at the core, thermocouple 2 at the surface

The heating profile through the thickness is an important aspect of the de-welding process. The modeled through thickness behavior is shown in Fig. 5.9, with the measured interface temp and surface temp as reference points. The model slightly underestimated the measured ΔT. Moreover, these plots illustrate the significant cooling effect of the aluminum heat sink and the effect of the glass fiber layer as a thermal barrier. Specifically, the peak interface temperature ($T_{interface}$) reaches 390°C, whereas the peak surface temperature ($T_{surface}$) is only 55°C.

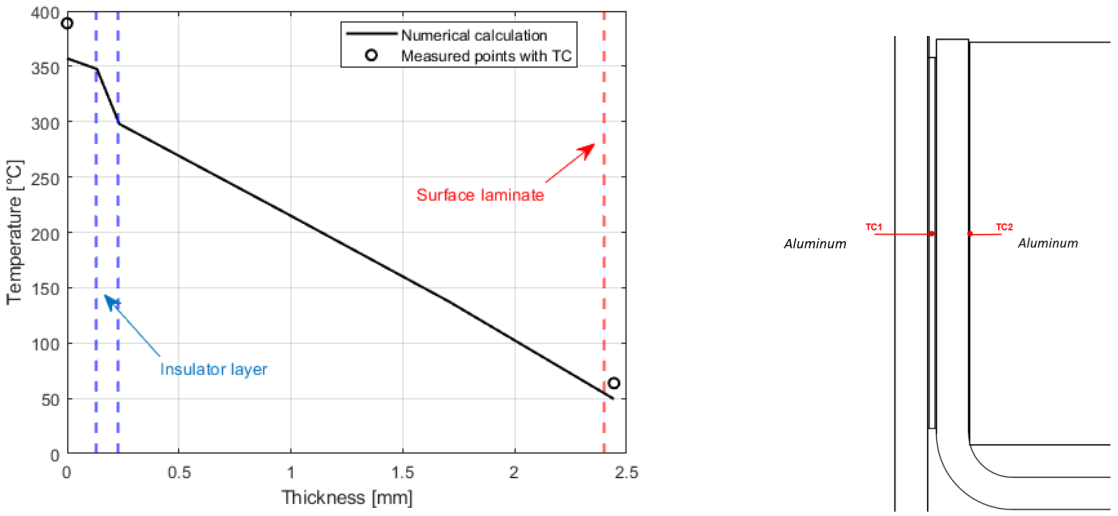

Figure 5.9: Left; Through thickness analysis L-pull-off specimen, numerical with measured data points, 25Volts t = 60 sec. Right; Schematic of the thermocouples, Thermocouple 1 at the core, thermocouple 2 at the surface

5.3.2. Results de-welding

This section addresses all experimental results of the L-pull-off specimens. First, all the results will be given as an overview. Subsequently, the fracture surfaces and the force and temperature curves with respect to time will be investigated individually for every specimen.

The test results are noted below in table 5.3. The remaining strength of the specimens was calculated using the maximum load and the weld area (25.4 x 80mm). The de-welding time took an average of 40 seconds. The force onto the specimen was applied when reaching the target temperature. The power density to reach melt temperature was averaged.

Number	Goal	Interface temp($^\circ$C)	Surface temp($^\circ$C)	Force	Strength	Heating time
Batch 1						
L Stiff 11	Reference	RT	RT	3.65 kN	1.8 Mpa	-
L Stiff 12	Reference	RT	RT	3.69 kN	1.82 Mpa	-
L Stiff 1	Above T_m	367	52	11 N	0.005 Mpa	30s
L Stiff 2	Above T_m	349	80	1 N	0.0001 Mpa	34s
L Stiff 3	Above T_m	304	50	103 N	0.05 Mpa	37s
L Stiff 4	Above T_m	410	105	76 N	0.037 Mpa	45s
L Stiff 5		219	48	450 N	0.16 Mpa	69s
L Stiff 6		243	100	470 N	0.24 Mpa	220s
L Stiff 7		250	51	730 N	0.37 Mpa	120s
L Stiff 8		245	55	1250 N	0.62 Mpa	-
L Stiff 9		249	48	1470 N	0.73 Mpa	-
Batch 2						
L Stiff 13	Reference	RT	RT	3.36 kN	1.65 Mpa	-
L Stiff 14	Reference	RT	RT	3.31 kN	1.63 Mpa	-
L Stiff 15	Above T_m	353*	128	1 N	0.0005 Mpa	60s
L Stiff 16	Above T_m	320*	85	220 N	0.11 Mpa	30s
L Stiff 17	Above T_m	348*	110	10 N	0.005 Mpa	55s
L Stiff 18	Above T_m	333*	85	280 N	0.14 Mpa	40s

Table 5.3: De-welding results. The interface temp with a star (*) is computed with the model. Specimens 8 and 9 were too strong to be de-welded at 245, and the maximum load recorded by the load cell is listed.

The results are graphically summarized in a strength temperature plot below in Fig. 5.10. The Figure illustrates the de-weld strength of the experiments, plotted against their respective temperature conditions. The bars represent the average strength, with error bars indicating the standard deviations.

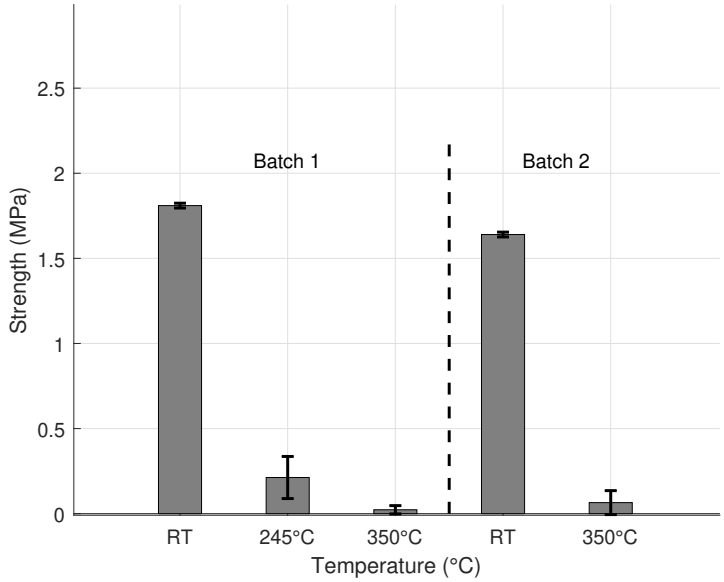

Figure 5.10: Strength vs temperature per specimen group, with standard dev. bars

Reference - Room temperature

Specimens 11 through 14 were tested at room temperature using a tensile test bench to determine their reference strength. These strengths are used to compare the forces acting during the de-welding process. The force-displacement curves for these specimens are displayed in Figure 5.11. The average ultimate failure load was 3.54 kN, with the highest strength 3.69 kN and the lowest 3.31 kN within 10 % of the average. The strength curves have different initial slopes because the constraint bars were not in contact with the specimen at the start of the experiment. As a result, the L-pull-off specimens were pulled until they made contact with the constraint bars, after which the slope increases.

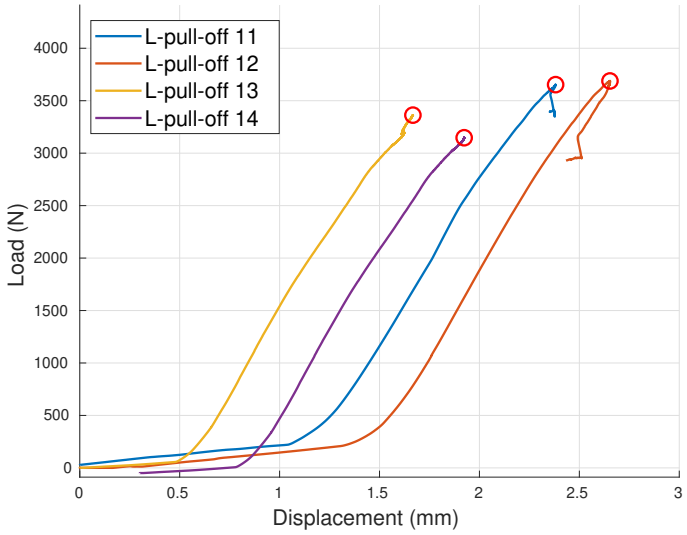

Figure 5.11: Force displacement curves of pull-off experiments, ASTM D7264, crosshead speed 1.00 mm/min, Support span (L) 40.0 mm

The fractured surfaces of the specimens are displayed in Figure 5.12 and 5.13. It can be seen that the specimens fail at the bottom glass fiber layer and partly at the flat skin bottom-adherend. Especially specimen 13 & 15, showcase fiber de-bonding from the upper plies of the flat skin. During the experiment is was observed that the stiffeners were peeled off in the glass fiber layer.

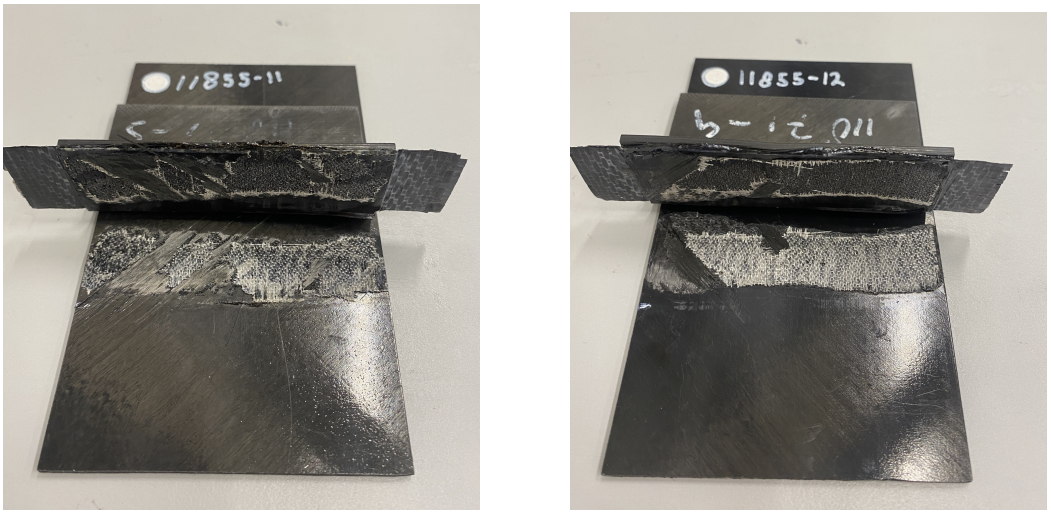

Figure 5.12: Fracture surface of reference specimens 11 and 12 tested at room temperature

Figure 5.13: Fracture surface of reference specimens 13 and 14 tested at room temperature

The fracture behavior is shown schematically in Fig. 5.14. The left sub-figure illustrates Mode I fracture, characterized by crack opening or tensile mode where the crack faces move directly apart. The schematic at the right shows the L stiffener with the forces acting on the specimen, leading to a crack propagation at an angle (peeling). These reference tests' constraints differed from those in the resistance de-weld setup. In this standard, one constraint is on top of the flange of the L-stiffener; in the designed setup, the constraints are both onto the flat laminate. Following the standard, this constraint on the L-stiffener contributes to the strength of the L-pull-off specimen.

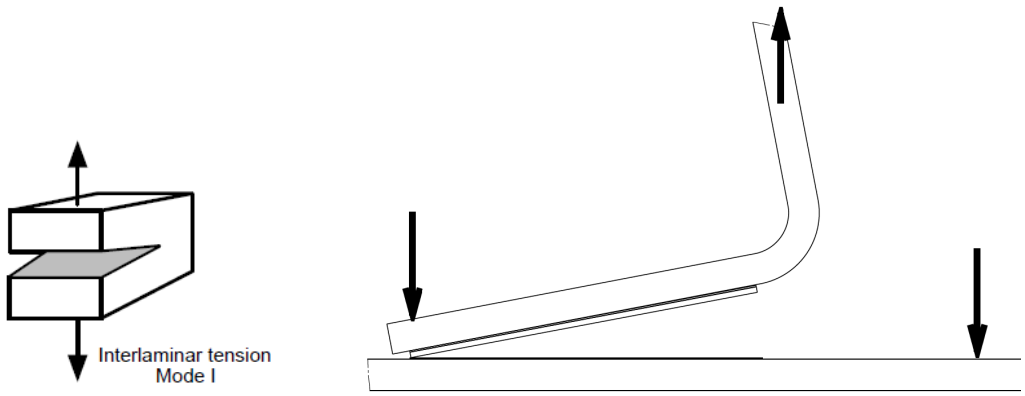

Figure 5.14: Fracture behaviour , left mode I [44], right visualization failing at glass fiber heating element interface

Melting temperature

The de-welding behaviour was characterized by monitoring the temperature at the interface and surface, as well as the load. This data provides insights into the thermal and mechanical behavior during the de-welding experiments. The L-pull-off specimens were analyzed individually with the load/temperature curve with a picture of the fracture surface. For good comparison, the axes are kept constant in the figures.

In Fig. 5.15, the load and temperatures are plotted over time, and the fracture surface after the de-weld experiment is displayed alongside. The interface reaches melt temperature quickly within 30 seconds, and the surface temperature slightly increases, highlighting the localized heating and cooling at the surface of the aluminum blocks. The load, shown in the Figure with an orange line, demonstrates a trend throughout the de-welding experiment. In the first phase, the load recorded by the load cell decreases; this suggests an outward pushing force of the specimen during the heating. This is due to the thermal expansion of the specimen, which is trying to expand and thus pushing harder against both aluminum blocks. After the interface reaches melt for a small period of time, the cylinder is excited to pull on the L stiffener, which is the peak in the curve. After this cycle, the specimen was de-welded, and the results are displayed alongside the plot. Specimen 1 in Fig.5.15 was disassembled at an interface temperature of approximately 360 °C, occurring at 31 seconds. Upon examination, no deconsolidation in the adherends was observed. The picture of the fractured surface shows that the heating element remains intact.

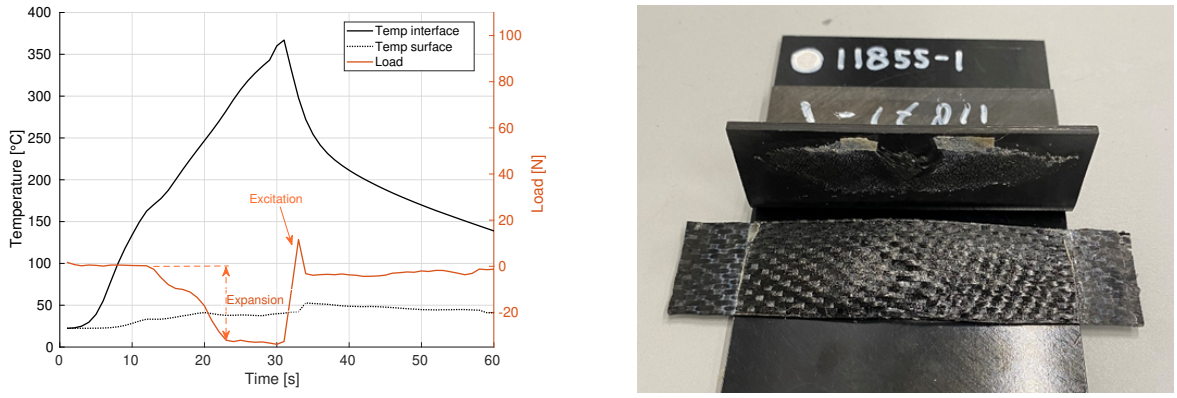

Figure 5.15: De-weld L stiff 1; Left Figure Load/interface temperature/surface temperature plotted with respect to time. Annotation is added by the specimen's expansion phase and at the Lstiffener's pull-excitation. Right Figure displays the fracture surface after de-welding (glass fiber layer lost during the process)

Specimen 2, displayed in Fig. 5.16, exhibited similar behavior to specimen 1. It was disassembled at an interface temperature of approximately 350 °C, occurring at around 31 seconds. As with specimen

1, no deconsolidation/delamination in the adherends was observed upon examination. The fracture surface of specimen 2 also showed an intact heating element, the glass insulator layer is burned and wrinkled as displayed in the Figure. The burning started when the L-stiffener moved from the flat plate.

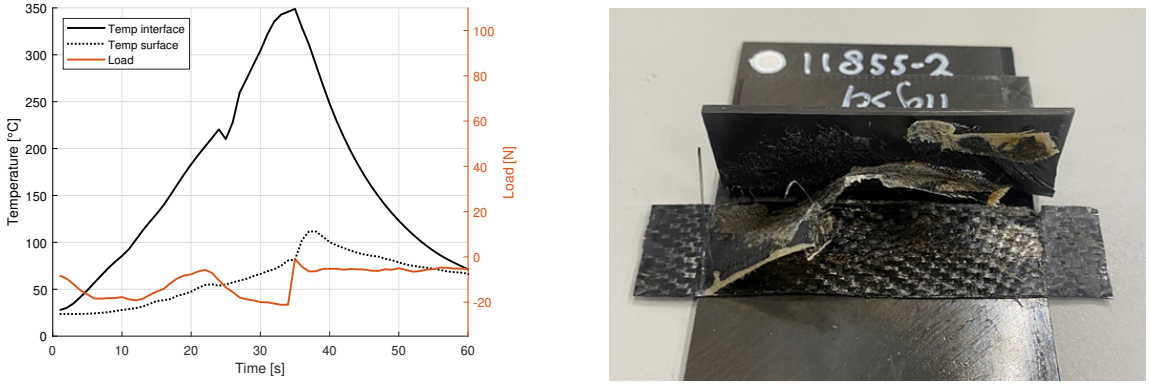

Figure 5.16: De-weld L stiff 2; Left Figure Load / interface temperature / surface temperature plotted with respect to time. Right Figure displays the fracture surface after de-welding.

In the case of specimen 3, the heating took longer compared to the previously described specimens. The force was applied after 37 seconds at an interface temperature of 305°C. The force required for disassembly at this temperature was considerably higher than specimens 1 & 2. The fracture surface shows that fibers were pulled from the woven carbon fiber heating element with the L-stiffener. This specimen showcases that the force was applied too early while the interface was not completely melted.

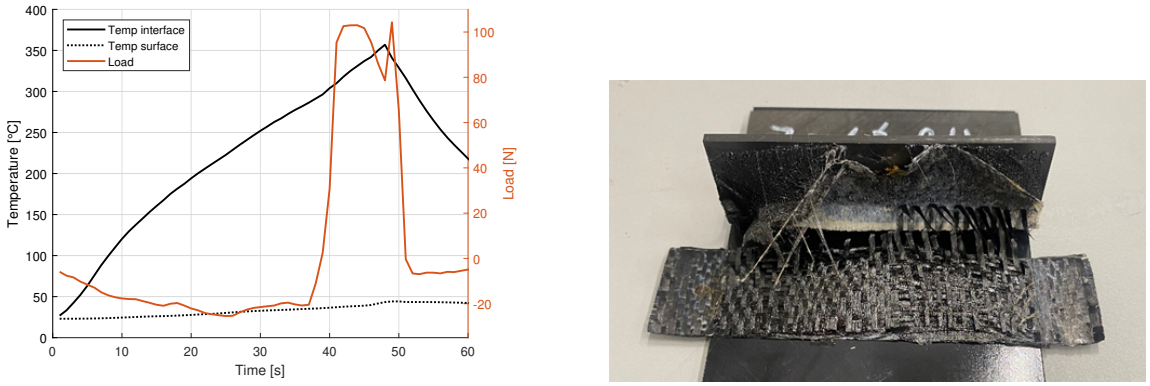

Figure 5.17: De-weld L stiff 3; Left Figure Load / interface temperature / surface temperature plotted with respect to time. Right Figure displays the fracture surface after de-welding.

Specimen 4, Fig. 5.18, was de-welded at a temperature high above the melt temperature, around 400 degrees Celsius. Upon examination, no deconsolidation in the adherends was observed. The picture of the fractured surface shows that the heating element remains intact.

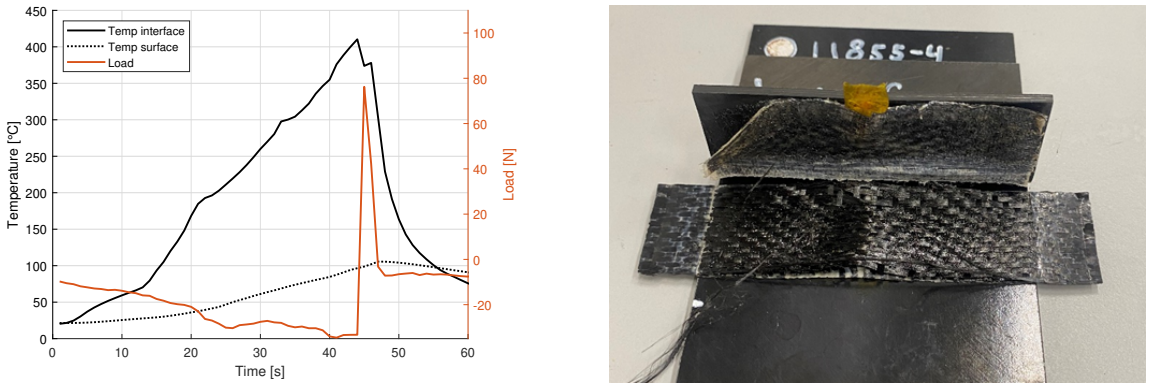

Figure 5.18: De-weld L stiff 4; Left Figure Load / interface temperature / surface temperature plotted with respect to time. The right Figure displays the fracture surface after de-welding.

Results without Thermocouple

This section presents specimens 15-18, which were tested without thermocouples. These specimens were monitored to determine the time required to reach the melt temperature.

Figure 5.19 shows the surface temperature and load during the de-welding process of the L-stiffener specimen 15. The surface temperature rises sharply, reaching 100°C at approximately 42 seconds. Disassembly began at a surface temperature of around 120°C, occurring at 60 seconds. At this point, the specimen exhibited almost no remaining strength. The fracture surface, shown on the right side of the figure, reveals delamination within the L-stiffener. The extended duration of the experiment suggests that the interface temperature likely exceeded the melt temperature, as indicated by the lack of residual strength and the data in Figure 5.8. The predicted interface temperature, calculated by the model, is 353 °C.

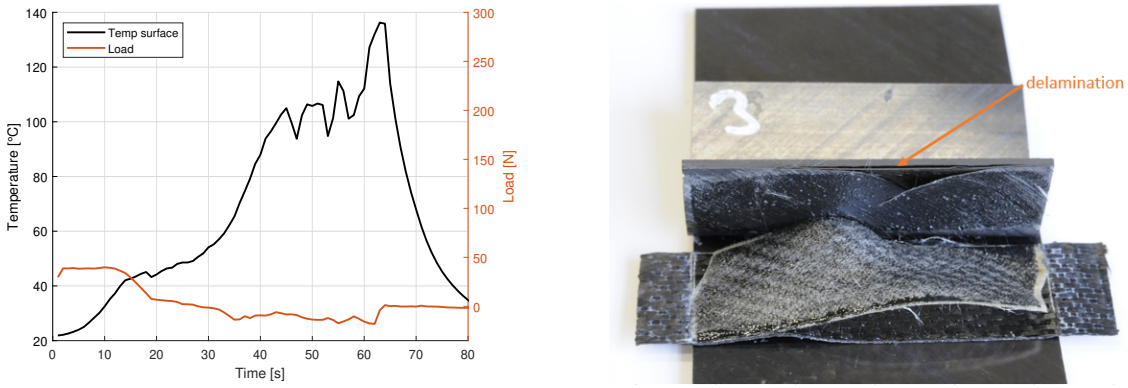

Figure 5.19: Deweld L stiff 15; Left Figure Load / surface temperature plotted with respect to time. Right Figure displays the fracture surface after de-welding

Specimen 16 (Figure 5.20): In this case, the force was applied too early at a relatively low temperature. The result was an incomplete de-weld with insufficient delamination, as shown in the fracture surface image. The premature application of force likely prevented the interface from reaching the optimal temperature, leading to a weaker separation.

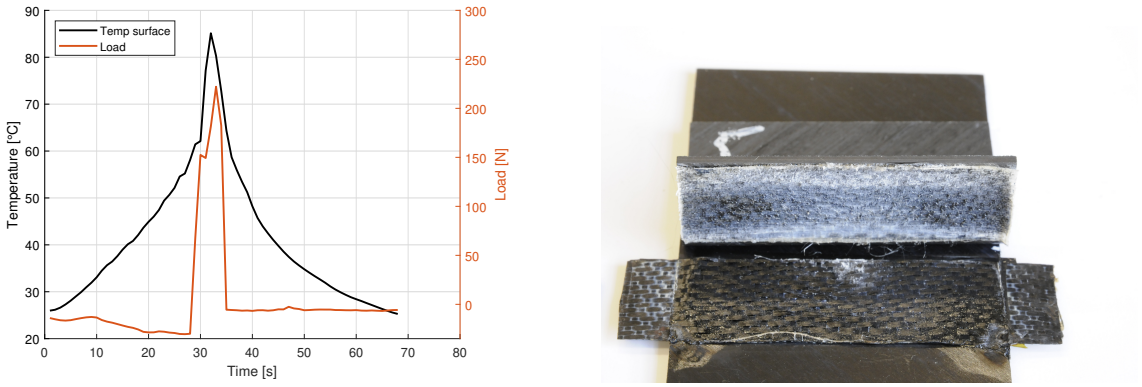

Figure 5.20: Deweld L stiff 16; Left figure Load / surface temperature plotted with respect to time. Right Figure displays the fracture surface after de-welding

Specimen 17 (Figure 5.21): Here, the experiment was prolonged too long, allowing the temperature to rise excessively. This overexposure resulted in a highly degraded interface, significantly weakening the material. The fracture surface confirms the excessive heating, where the material likely exceeded its melt temperature, leading to an extensive loss of structural integrity.

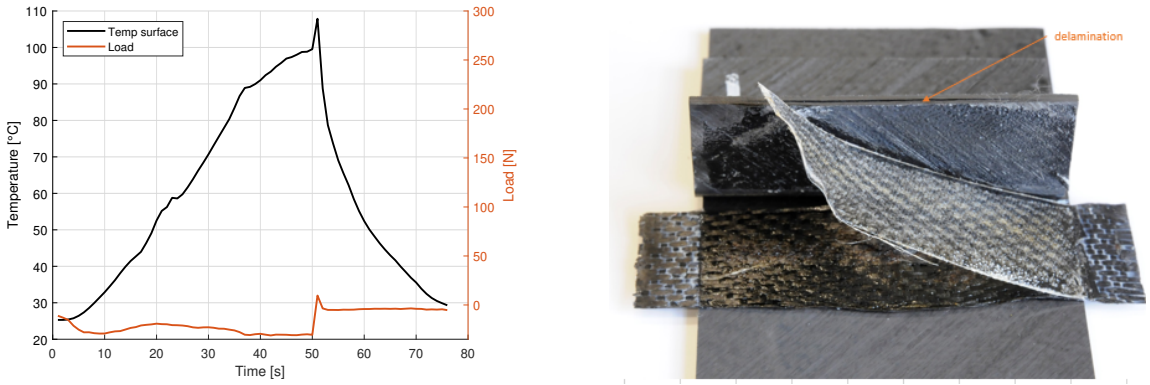

Figure 5.21: Deweld L stiff 17; Left figure Load / surface temperature plotted with respect to time. Right Figure displays the fracture surface after de-welding

Specimen 18 (Figure 5.22): This specimen represents a near-perfect de-weld process. The force was applied at the correct moment, and the temperature was well-controlled, leading to an ideal separation with minimal material degradation. The fracture surface shows a clean delamination, indicating that the de-welding was performed under optimal conditions.

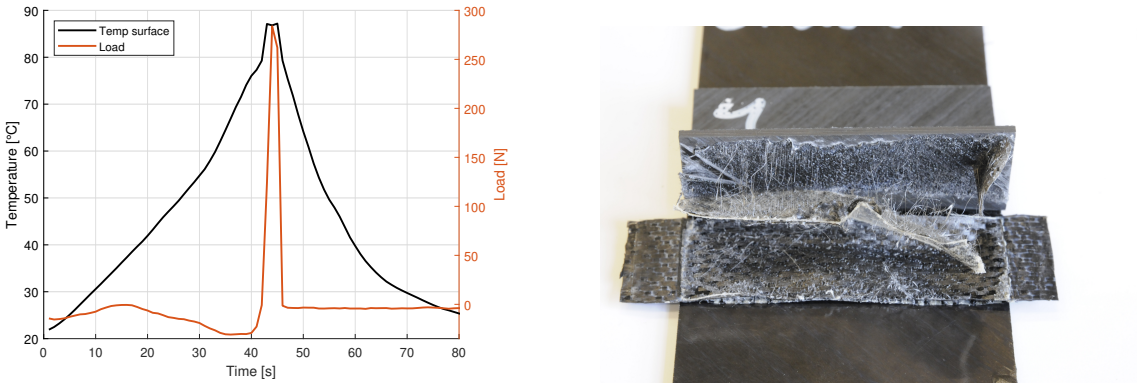

Figure 5.22: Deweld L stiff 18; Left figure Load / surface temperature plotted with respect to time. Right Figure displays the fracture surface after de-welding

Tests at 245°C

Specimens 5-9 were tested at a temperature of 245 ± 10 °C.

Specimen 5 (Figure 5.23): This specimen was subjected to a lower temperature, resulting in a significantly higher force required for de-welding than previous tests. Interestingly, no consolidation occurred in the middle section of the specimen, as shown in the Figure. This suggests that, during welding, the temperature may have been insufficient to achieve complete bonding across the entire interface, leading to an uneven de-welding process.

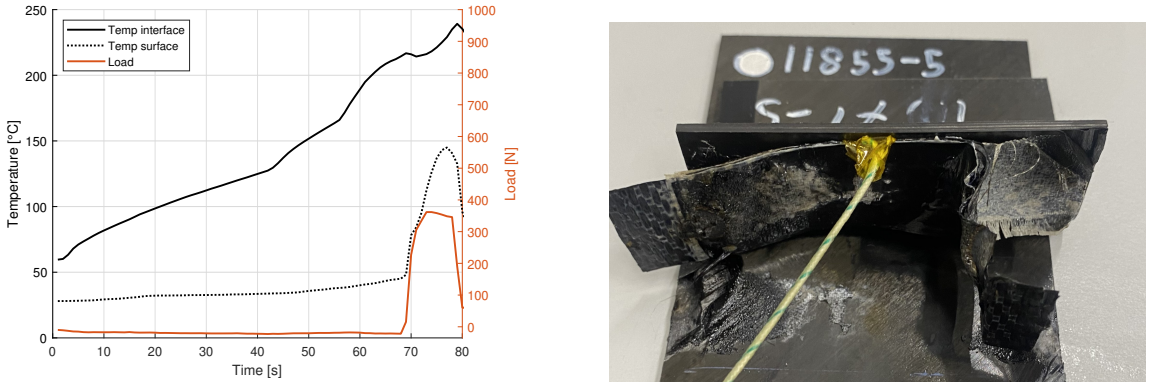

Figure 5.23: Deweld L stiff 5

Specimens 6 and 7 (Figures 5.24 and 5.25): These specimens exhibited comparable de-welding behaviour. Both displayed fracture surfaces where the fibers were broken off from the heating element, indicating that the applied force during the de-welding process was sufficient to separate the fibers. The similarity in their fracture surfaces suggests that the de-welding conditions were consistent, leading to a uniform failure mode in both specimens.

In Fig. 5.25, the load application applied in steps can be seen. The force increased step-wise until disassembly was achieved.

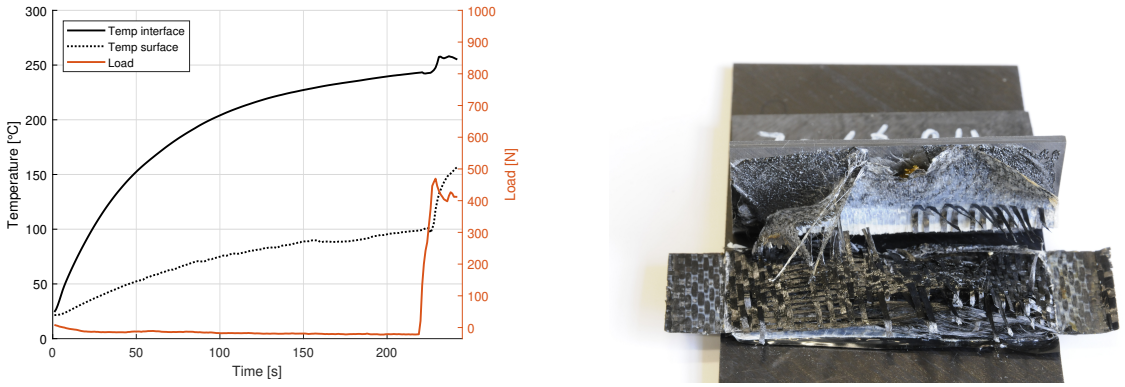

Figure 5.24: Deweld L stiff 6; Left figure Load / surface temperature plotted with respect to time. Right Figure displays the fracture surface after de-welding

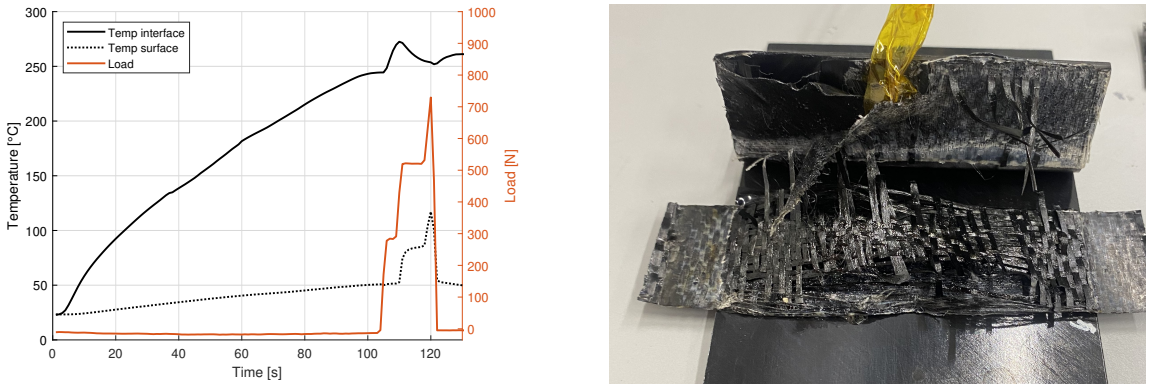

Figure 5.25: Deweld L stiff 7 Left figure Load / surface temperature plotted with respect to time. Right Figure displays the fracture surface after de-welding

Specimens 8 and 9 could not be de-welded in the test bench due to the remaining strength in the weld. The maximum loads recorded on the specimens were 1250N and 1470 N, respectively. The constraint bar in the test bench could not handle a higher load, so the de-weld experiment had to stop before separation. Nevertheless, it can be seen that the strength at this temperature for these specimens is high, which is not unexpected because melting is not initiated.

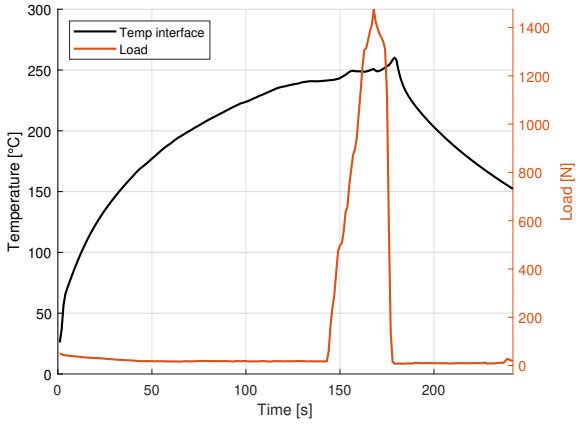

Figure 5.26: Deweld figure L stiff 9, the stiffener could not be disassembled

5.3.3. Conclusion L-pull-off experiments

The individual analysis of the L pull-off specimens reveals several key observations and trends.

Firstly, the data shows a clear correlation between interface temperature and the force required for de-welding (see Fig. 5.10. At room temperature, the reference specimens (11-14) exhibited consistent strengths with minimal scatter. This consistency indicates that at room temperature temperatures, the material's strength is reliably maintained, resulting in predictable failure modes. The intermediate temperature of 245°C in batch 1 shows a different result, illustrating a considerable scatter of remaining joint strength. The fracture behaviors show a heating element with fibers pulled out. As the interface temperature increased, the de-welding forces decreased to almost zero, as observed in specimens 1-4 in batch 1 and specimens 15-18 in batch 2. The latter showed that timing of the load application is essential; slightly too early results in higher forces and too late in deconsolidation in the adherends. The zero-strength de-weld observed above the melt temperature indicates that the interface was sufficiently molten, allowing most molecular chains to remain unbroken.

Based on these observations, it is recommended that de-welding processes should aim for a controlled interface temperature, within the range of 320-350°C, and precise timing of force application to ensure effective de-welding without affecting the adherends properties too much.

Due to the force applications of the connector blocks, the resistance heating element stayed on the flat plate for all experiments and consolidated right after the experiments to this. The heating elements showed minimal degradation after de-welding at the melt temperature, indicating that the process did not significantly affect their integrity. From a practical standpoint, it may be undesirable that the heating element immediately consolidates on the flat plat, especially if repositioning or recycling is required. However, with the heating element remaining mostly intact, it appears that re-weldability of the L-stiffeners is a viable option.

6

Discussion

The discussion of the results is done by following the structure of the results chapter: Model, SLS experiments, and L-pull-off experiments. At last, the differences between SLS and L-pull-off are discussed.

6.1. Model

It was found that the model showed average convergence with the experimental data and worked well and efficiently, taking around two minutes per simulation. However, the model can be improved by the following. The experiments were controlled by constant power, and the model had an input of power density (W/m^2); due to the high sensitivity (see Fig. 5.3) of the power input, this has to be accurate. The currents were tracked by recording the voltages and currents displayed by the power source by camera. The data from this video was listed on a five-second period base. It would be better if this frequency of data measurement could be higher, with a more exact power output of the source. Moreover, the power losses in the cable and due to contact resistances must be measured; when incorporating this, better results could be expected.

Regarding the properties of the FEM model, the heat transfer coefficient of natural convection at the boundary of the model could be improved. Calculating or measuring the heat transfer coefficient for a vertical flat surface with these dimensions at elevated temperatures would be helpful.

6.2. SLS

Since the co-consolidated joints are rather uniform in quality, the number of specimens (three per temperature) was sufficient to draw conclusions. Nevertheless, one main source of uncertainty was identified regarding the non-uniformity of the heating area.

The surface temperature was averaged over a circular area using an infrared camera during the SLS de-welding experiments. The temperature was measured and averaged for a circular region in the center of the interface, shown in Fig. 6.1. During the experiments, it was noted that the temperature difference across the SLS surface was significant. In figure 6.1, an example is given for the average 195-degree surface temperature; due to the edge effect (yellow section), the temperature above in the circle is approximately three degrees warmer at the bottom of the circle it is the opposite.

A result of this non-uniformity is that the strength temperature plot of figure 5.6 is for the middle point at the surface.

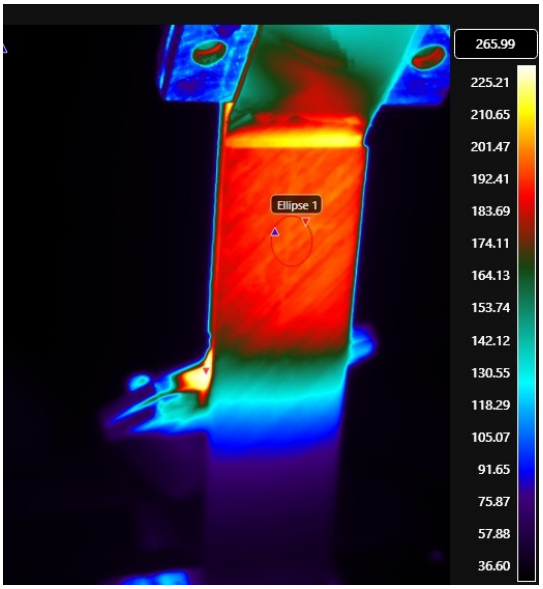

Figure 6.1: IR image of the SLS specimen - 195 degree of averaged surface temperature

Comparison LMPEAK versus PEI interface

Previously NLR ([13]) tested the de-welding of SLS specimens with LMPEAK interlayer. This de-welding experiment was performed with a thinner LMPEAK glass insulator layer. As described, the insulator layer, which prevents the electricity from flowing through the laminates, also acts as a thermal insulator. The PEI glass insulator ($0.24mm$) was twice as thick as the previously used LMPEAK glass insulator ($0.12mm$). In Fig. 6.2, the through-thickness profiles of these specimens are plotted numerically. As this figure illustrates, the thicker PEI glass fiber layer improves the thermal barrier for the adherends, which is beneficial for the de-weld process.

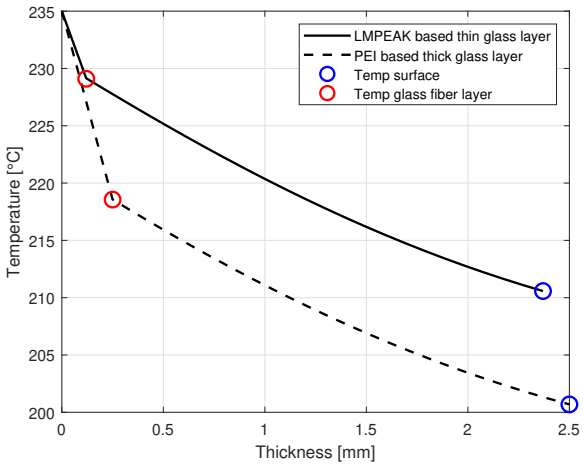

Figure 6.2: Through thickness comparison - PEI vs PEAK at 235°C interface temperature

The result of the de-welding with a thinner LMPEAK interlayer is shown in Fig. 6.3, next to the results of the specimens with PEI interlayer obtained in this thesis. Comparing both graphs, it becomes clear that the semi-crystalline LMPEAK behaves differently than the amorphous PEI. After the glass temperature of LMPEAK 134-158 °C, the strength of the joints exhibits a more gradual decline over a wider temperature range.

This difference in behavior is attributed to the molecular structure of semi-crystalline polymers. Unlike amorphous polymers, semi-crystalline polymers retain ordered crystalline regions which decline after

their glass transition temperature (T_g) [1]. These crystalline domains provide additional mechanical strength and stability, allowing the material to maintain its integrity over a broader temperature range. In contrast, amorphous polymers like PEI soften significantly upon reaching T_g, leading to a rapid decline in mechanical strength as there is no crystalline phase to reinforce the material.

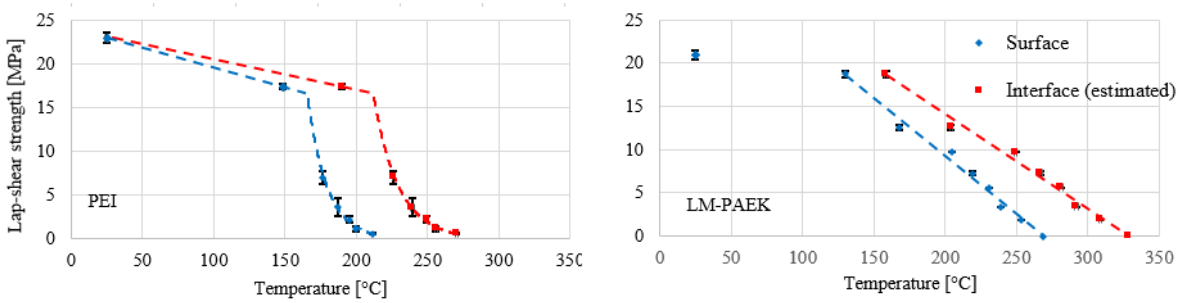

Figure 6.3: SLS strength at various surface and estimated interface temperatures, Left replicate of Fig. 5.6 and right graph from [13]

The observed behavior during the SLS de-welding experiments makes PEI an interesting material for joining LM-PAEK matrix composites. Due to the problem linked to PEI's chemical resistance, such a technology is unlikely to find its way into structural components in aerospace but could be of aircraft interiors. [13]

6.3. L-pull-off

The de-welding of the L-pull-off specimens had more uncertainties compared to the SLS coupons. At first, the specimens were produced by resistance welding on the developed test bench. Every specimen had different welding parameters (see Appendix B), resulting in weld-quality differences throughout the specimens. So, the input of the experiments was not perfectly known. For further research, adding a quality check (c-scan or microscopy) between the welding and de-welding would be beneficial to ensure approximately the same quality specimens.

During the welding of the L-pull-off specimens, it was noted that the pressure on the weld stack was not completely uniform. This was primarily because of the 'thick' k-type thermocouple at the interface and surface of the laminates in the first batch. Moreover, the alignment of the upper heat sink was done by hand, adding extra uncertainty in the repeatability throughout the specimens. A shaft must guide the heat sink for consistent and reliable pressure, and no thermocouple must be in the weld stack. These uncertainties result in a different heating behavior throughout specimens; such a difference is shown in Fig. 6.4 as an example; in further research, it would be useful to analyze and narrow this bandwidth.

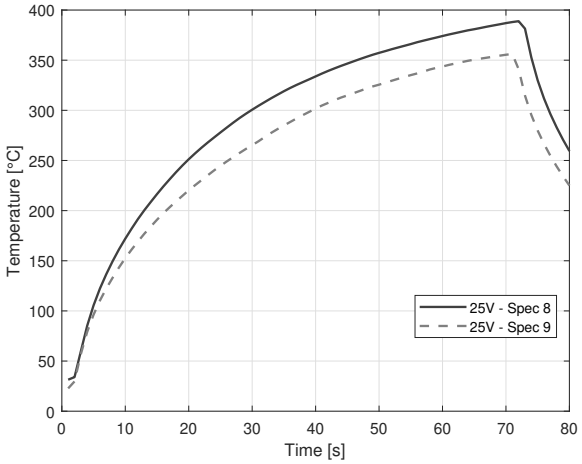

Figure 6.4: Illustration repeatability, different heating profile for specimen 8 & 9 for a constant 25V case

As described in chapter 3, the force of the pneumatic cylinder was manually controlled using a Festo pneumatic regulator by turning the knob by hand and reading the analog pressure gauge. Also, the speed of the pneumatic cylinder could not be controlled. This resulted in an inconsistent load application, with different velocities. The strength of a polymer depends on the strain rate, and by using a creep- or tensile test bench, this could be controlled [53]. Like in the study of de Weert [11], where disassembly experiments were performed by applying a fixed force with weight in a creep bench. In this bench, a fixed displacement rate of 1mm per minute could be applied following standard ASTM D-1002. This standard was also followed in the study of Ageorges [25].

Also, the power source is controlled by hand, adding extra uncertainty. A controllable power source will instantly increase the repeatability of the de-welding experiments.

The matrix removal is done by burning the matrix off by hand with an ultrasonic device to improve the electrical connector's contact with the carbon fibers. Although this process is not considered to have a significant impact, it is recommended that a standardized procedure be established to ensure a more consistent and uniform quality of the heating element.

It can be concluded that de-welding for a L-pull-off specimen in between two heat sinks is energy-intensive. For rapid de-welding under the given conditions, a power density of approximately 170 kW/m² is required, driven by a power input of 475 W, which is relatively high, as discussed in Chapter 2. Regarding scalability, considering a longer weld of 1 meter, which is approximately ten times longer than the weld in the L-pull-off specimens, the power requirement increases proportionally, requiring a ten times bigger power source of around 4750 W. Table 6.1 below, illustrates how power consumption scales with increasing weld area. The table shows power consumption scales linearly with the weld area to maintain the same power density of 170 kW/m².

Weld Length (m)	Weld Area (m²)	Power Density (kW/m²)	Power Input (W)
0.1 (tested)	0.0028	170	475
0.5	0.014	170	2375
1.0	0.028	170	4750
2.0	0.056	170	9500

Table 6.1: Increase in Power Consumption with Weld Area

6.4. Comparison SLS versus L-pull off

The de-welding experiments were performed on co-consolidated (SLS) and resistance-welded (L-pull off) specimens. The difference in the de-welding experiments is large due to the geometry, load application, and consolidation type, making it hard to compare them. The SLS experiments were a more quantitative study on the reduction of force against interface temperature compared to a more qualitative study on the de-welding of the L-pull-off specimens.

However, based on the experiments, the most logical strategy seems to be de-welding in an out-of-plane direction.

7

Conclusion

In this last chapter, the thesis will be concluded by assessing the objective and requirements defined in Chapter 1 and giving an overall conclusion for this work. Finally, recommendations for future work will be given in the last section.

This study researched the feasibility of the thermoplastic composites de-welding process by resistance heating. Resistance de-welding was demonstrated to be feasible for the tested types of geometries and dimensions concerning the requirements. The de-welding process appeared to be very successful in lowering the required disassembly force by heating the interface, for both Single lap shear testing and L-pull-off experiments. The adherends showed no delamination when using a heat sink and insulator layer. During the L-pull-off de-welding the heat sink played the most crucial role in protecting the adherend from thermal damage by cooling the adherend significantly. Regarding the insulator layer, it was shown that de-welding without such a layer is not feasible due to the critical thermal protection it offers. The heating elements remained intact during the L-pull-off experiments; during the SLS test, the 'edge effect' burned and permanently damaged the heating elements.

More specific conclusions are listed below;

- An Abaqus finite element model was developed, with the resistance heating mechanism incorporated to predict the temperatures during de-welding. The model was simplified to a laminate with heat generation inside at the location of the heating element. It predicts the temperature within 10%, but showed higher heating and cooling rates than measured.
- The strength of the SLS specimens was tested at various temperatures, 'Zero strength' and good de-welds were observed at temperatures above the glass transition temperature of PEI. Higher temperatures are possible, in theory, up to 305°C, when damage in the LM-PAEK matrix adherends can be expected. However, from a purely de-welding perspective, heating beyond the zero-strength point of 250°C serves no purpose and only increases energy consumption. The PEI interlayer showed the use of enlarging the process window for de-welding. The observed behaviour during the SLS de-welding experiments, makes PEI an interesting material for joining LM-PAEK matrix composite with de-welding capabilities.
- The L-pull-off experiments, through a more qualitative experiment, showed that good de-welding happens above the melt temperature of LM-PEAK. The results showed that almost no strength remained after heating the interface to 345°C. The heating element remained intact after de-welding at these temperatures; at lower de-welding temperatures, this element was ripped apart.
- It is demonstrated that the energy consumption for de-welding the L-pull off specimens is high, mainly due to the application of heat sinks. A high power density is required for a short duration to achieve a fast de-weld with minimal impact on the adherend. The power requirement increases proportionally with the weld's length and/or width, quickly leading to substantial demands. The de-welding of L stiffeners under these conditions seems only feasible for weld lengths up to one meter while maintaining a constant width. De-welding beyond this area will require high-power

welding operations.

Having stated the conclusions, it is worth noting that the weld quality of the L-stiffened skins could have influenced the de-welding process. The quality of the L-pull-off specimens was not constant and was difficult to assess, resulting in an unknown input to the de-welding experiments. The scatter introduced while manufacturing (welding) these specimens could be more accurate to improve the validity of these results.

During this research, some ideas came up about possibilities for further research. The following recommendations are given:

- The consistency of resistance heating could be improved significantly by using a programmable/-controllable power source.
- The de-welded specimens evaluating for re-weldability, to determine if re-assembly is feasible.
- De-welding with larger and more complex shapes to find out boundaries. Incorporating curvature of a fuselage skin
- Microscopy on the adherends, in this research, the specimens were visually checked for delamination defects, but delamination may have occurred, which is not visually by the eye.
- Another viable de-welding technique can be peeling force with induction heating.

References

[1] Ali Yousefpour, Mehdi Hojjati, and Jean-Pierre Immarigeon. “Fusion Bonding/Welding of Thermoplastic Composites”. In: *Journal of Thermoplastic Composite Materials* 17.4 (2004), pp. 303–341. DOI: 10.1177/0892705704045187.

[2] Ana Diez-Pascual et al. “Multiscale fiber-reinforced thermoplastic composites incorporating carbon nanotubes: A review”. In: *Current Opinion in Solid State and Materials Science* 18 (Jan. 2013). DOI: 10.1016/j.cossms.2013.06.003.

[3] Alfred C. Loos and Min-Chung Li. “Non-isothermal autohesion model for amorphous thermoplastic composites”. In: *Journal of Thermoplastic Composite Materials* 7.4 (1994), pp. 280–310.

[4] Huaji Shi. “Resistance welding of thermoplastic composites: Process and performance”. PhD thesis. TU Delft, 2014. URL: https://resolver.tudelft.nl/uuid:58f16f99-afc1-4713-842e-562412583340.

[5] B. Sarh, W. G. Roeseler, and M. U. Kismarton. “Composite structures: The first 100 years”. In: *ICCM International Conferences on Composite Materials*. 2007.

[6] Ali Yousefpour, Mehdi Hojjati, and Jean-Pierre Immarigeon. “Fusion Bonding/Welding of Thermoplastic Composites”. In: *Journal of Thermoplastic Composite Materials* 17.4 (2004), pp. 303–341.

[7] Xuhai Xiong et al. “Resistance welding technology of fiber reinforced polymer composites: a review”. In: *Journal of Adhesion Science* (2020). DOI: 10.1080/01694243.2020.1856514.

[8] Manuel Endrass et al. “Resistance welding of low-melt polyaryletherketone: Process definition and optimization”. In: *DLR and AIRBUS* (2022).

[9] C. Kassapoglou. *Design and Analysis of Composite Structures with Applications to Aerospace Structures*. The Netherlands: Delft University of Technology, 2010.

[10] Eric R. Johnson and Naveen Rastogi. *Load Transfer in the Stiffener-To-Skin Joints of a Pressurized Fuselage*. Technical Report VPI-E-95-01. NASA Grant NAG-1-537, Performance Period: November 1, 1991 to April 30, 1995. National Aeronautics and Space Administration, Langley Research Center: Department of Aerospace and Ocean Engineering, May 1995.

[11] Loïc De Weert. “Disassembly of fusion bonded thermoplastic composite joints aided by induction heating”. In: (2021). URL: https://resolver.tudelft.nl/uuid:134a76c4-ca1c-499d-a6da-403546d50c6f.

[12] Harry Frederick, Wencai Li, and Genevieve Palardy. “Disassembly Study of Ultrasonically Welded Thermoplastic Composite Joints via Resistance Heating”. In: *Materials* (2021). URL: https://www.mdpi.com/1996-1944/14/10/2521.

[13] C. de Vos et al. “De-welding of thermoplastic composites: next step in sustainable joints”. In: *NXTGEN HIGHTECH* (2024).

[14] Max U. Kismarton William G. Roeseler Branko Sarh. “COMPOSITE STRUCTURES: THE FIRST 100 YEARS”. In: *16TH INTERNATIONAL CONFERENCE ON COMPOSITE MATERIALS* (2007). URL: https://www.iccm-central.org/Proceedings/ICCM16proceedings/contents/pdf/MonA/MoAM1-01sp_roeselerw228184p.pdf.

[15] Yannick van der Wilt. “Conduction Welding of Thermoplastic Composites: An Experimental Study Towards Specifying the Process Window for Process Time and Temperature”. Master’s thesis. Enschede, The Netherlands: University of Twente, Aug. 2024.

[16] J. Barroeta Robles et al. “Repair of thermoplastic composites: an overview”. In: *Advanced Manufacturing: Polymer & Composites Science* (2022).

[17] M Hou, L Ye, and YW Mai. “An experimental study of resistance welding of carbon fibre fabric reinforced polyetherimide (CF Fabric/PEI) composite material”. In: *Applied Composite Materials* 6 (1999), pp. 35–49.

[18] C. Ageorges, L. Ye, and M. Hou. “Advances in fusion bonding techniques for joining thermoplastic matrix composites: a review”. In: *Composites Part A: Applied Science and Manufacturing* 32.6 (2001), pp. 839–857. ISSN: 1359-835X. DOI: https://doi.org/10.1016/S1359-835X(00)00166-4. URL: https://www.sciencedirect.com/science/article/pii/S1359835X00001664.

[19] URL: https://www.compositesworld.com/articles/peek-vs-pekk-vs-paek-and-continuous-compression-molding.

[20] D. Stavrov and H.E.N. Bersee. “Resistance welding of thermoplastic composites - an overview”. In: *Composites Part A: Applied Science and Manufacturing* (2005). ISSN: 1359-835X.

[21] Christophe Ageorges et al. “Characteristics of resistance welding of lap shear coupons: Part II. Consolidation”. In: *Composites Part A: Applied Science and Manufacturing* 29.8 (1998), pp. 911–919.

[22] Chris Ageorges, Lin Ye, and M. Hou. “Advances in fusion bonding techniques for joining thermoplastic matrix composites: A review”. In: *Composites Part A: Applied Science and Manufacturing* 32 (June 2001), pp. 839–857. DOI: 10.1016/S1359-835X(00)00166-4.

[23] Manuel Endrass et al. “Towards continuous resistance welding for full-scale aerospace components”. In: *DLR with National Research Council Canada (NRC)* (2020).

[24] Przemysław Dobrzański. “Bonding of High Temperature Thermoplastic Carbon Composites with Resistance Welding Technique”. In: *Transactions on Aerospace Research* 2018 (2018), pp. 1–13. URL: https://api.semanticscholar.org/CorpusID:198963724.

[25] C Ageorges, L Ye, and M Hou. “Experimental investigation of the resistance welding for thermoplastic-matrix composites. Part I: heating element and heat transfer”. In: *Composites Science and Technology* 60 (2000), pp. 1027–1039.

[26] Anahi Pereira da Costa and Edson Cocchieri Botelho. “A Review of Welding Technologies for Thermoplastic Composites in Aerospace Applications”. In: *ICCM International Conferences on Composite Materials*. 2012.

[27] M. Hou, L. Ye, and Y.-W. Mai. “Resistance welding of carbon fibre fabric reinforced polyetherimide (CF fabric/PEI) composite material”. In: (2023).

[28] Edith Talbot. “Manufacturing process modelling of thermoplastic composite resistance welding”. In: (June 2005).

[29] Irene Fernandez Villegas and Harald EN Bersee. “Characterisation of a metal mesh heating element for closed-loop resistance welding of thermoplastic composites”. In: *Journal of Thermoplastic Composite Materials* 28.1 (2015), pp. 46–65. DOI: 10.1177/0892705712475012.

[30] Allard Wiebenga. “Induction and resistance welded repairs on thermoplastic composites”. In: (2020).

[31] S. McKnight et al. “Scaling Issues in Resistance-Welded Thermoplastic Composite Joints”. In: *Advances in Polymer Technology* 16.4 (1997).

[32] Wencai Li. “Investigation of welding repair methods for thermoplastic composite joints”. In: (2023).

[33] Mehrshad Moghadamazad and Suong. Hoa. *Models for heat transfer in thermoplastic composites made by automated fiber placement using Hot Gas Torch*. Dec. 2021. URL: https://www.sciencedirect.com/science/article/pii/S2666682021001067.

[34] Sofía Delgado Labrandero. “Characterization of metallic meshes used for resistance welding of thermoplastic composites”. MA thesis. 2009.

[35] Huajie Shi, Irene Fernandez Villegas, and Harald Bersee. “Analysis of void formation in thermoplastic composites during resistance welding”. In: *TU Delft* (2016).

[36] Erik Dahlm, Helmut Schürmann, and Christian Mittelstedt. “A tailored heating element for resistance welding of complex shaped joining surfaces”. In: (2022).

[37] Manuel Endrass et al. “Towards increased reliability of resistance welded joints for aircraft assembly”. In: *DLR and AIRBUS* (2020).

[38] João Pedro Reis, Marcelo de Moura, and Sylwester Samborski. “Thermoplastic Composites and Their Promising Applications in Joining and Repair Composites Structures: A Review”. In: (2020).

[39] E.SILVERMAN and R.GRIESE. “Joining methods for graphite/PEEK thermoplastic composites”. In: *Sampe Journal* 25 (1989), pp. 34–38.

[40] G. Crevecoeur and G. Groeninckx. “Binary blends of poly(ether ether ketone) and poly(ether imide): miscibility, crystallization behavior and semicrystalline morphology”. In: *Macromolecules* 24.5 (1991), pp. 1190–1195. DOI: 10.1021/ma00005a034. eprint: https://doi.org/10.1021/ma00005a034. URL: https://doi.org/10.1021/ma00005a034.

[41] A. J. Smiley et al. “Dual polymer bonding of thermoplastic composite structures”. In: *Polymer Engineering & Science* 31.7 (1991), pp. 526–532. DOI: https://doi.org/10.1002/pen.760310709. eprint: https://4spepublications.onlinelibrary.wiley.com/doi/pdf/10.1002/pen.760310709. URL: https://4spepublications.onlinelibrary.wiley.com/doi/abs/10.1002/pen.760310709.

[42] John W. McLaughlin, Emma Tobin, and Ronan M. O’Higgins. “An investigation of Polyether Imide (PEI) toughening of carbon fibre-reinforced Polyether Ether Ketone (PEEK) laminates”. In: *Materials & Design* 212 (2021), p. 110189. ISSN: 0264-1275. DOI: https://doi.org/10.1016/j.matdes.2021.110189. URL: https://www.sciencedirect.com/science/article/pii/S0264127521007449.

[43] David Dillard. *Advances in structural adhesive bonding*. Mar. 2010, pp. 1–637.

[44] M.G. van Dijk. “Induction Welded Unidirectional Carbon Fiber Reinforced Thermoplastic L-Joints”. In: (2019). URL: https://resolver.tudelft.nl/uuid:264cfd01-b8d2-4ea9-a8eb-bddf9d957615.

[45] RC Don, JW Gillespie Jr., and CLT Lambing. “Experimental characterization of processing-performance relationship of resistance welded graphite/Polyetheretherketone Composite Joints”. In: *Polymer Engineering and Science* 32 (1992), pp. 621–631.

[46] N. Koutras, R. Benedictus, and I. Fernandez Villegas. “Thermal effects on thermoplastic composites welded joints: A physical and mechanical characterisation”. PhD thesis. Delft University of Technology, 2020. URL: https://repository.tudelft.nl/islandora/object/uuid%3A8bdf06e6-8e42-463a-af45-20a56e0e2022?collection=research.

[47] Airbus. *Airbus standard RE1801807 L-Pull Static Testing of Welded Joints*. Reference 2. n.d.

[48] A. Zhang and Y. Li. “Thermal Conductivity of Aluminum Alloys-A Review”. In: *Materials (Basel, Switzerland)* 16.8 (2023), p. 2972. DOI: 10.3390/ma16082972. URL: https://doi.org/10.3390/ma16082972.

[49] Tim P.A. Koenis et al. “A Machine Learning Approach to Dynamic Simulation of Electromagnetic Heating”. In: (2023).

[50] Márton Farkas. “Reliable specific heat capacity measurements of thermoplastic composites with differential scanning calorimetry”. Master’s thesis. Department of Mechanical Engineering: University Name, 2021.

[51] Jitha S. Jayan et al. “An introduction to fiber reinforced composite materials”. In: (2021), pp. 1–24. DOI: 10.1016/b978-0-12-821090-1.00025-9. URL: https://doi.org/10.1016/b978-0-12-821090-1.00025-9.

[52] Wouter J.B. Grouve. “Weld strength of laser-assisted tape-placed thermoplastic composites”. English. PhD Thesis - Research UT, graduation UT. Netherlands: University of Twente, Aug. 2012. ISBN: 9789036533928. DOI: 10.3990/1.9789036533928.

[53] Ozan Erartsin. “Time-dependent, matrix-dominated failure of continuous fiber-reinforced thermoplastic composites”. English. PhD Thesis - Research UT, graduation UT. Netherlands: University of Twente, May 2020. ISBN: 978-90-365-4992-9. DOI: 10.3990/1.9789036549929.

A

Steady state simulations

Abaqus steady state calculation

This document describes the steady state simulation for determining the interface-surface correlation.

Properties – input

The following table states the general properties of the glass fiber-and UD carbon fiber layers obtained by toray[1]:

Material	Thickness	Resin Weight fraction	Volume fraction	Fiber Areal wheight	density
CF/lm Peak UD	0.14mm	34%		145 g/m2	1,59 g/cm3
GF/ lm peak (8 harness)	0.24mm	34%	0.52%	296 g/m2	1,92 g/cm3

The following properties are the input parameters for the Abaqus model. The specific heat capacity depends a lot on the temperature.

Section	Conductivity through thickness (W/mk)	Thickness	Specific heat capacity (J/kg K)
CF/lm Peak laminate	0.72 at 20C 0.91 at 200c	2.2mm	Range: 900 – 2000 (Farkas,2023)
Gf/ lm peak 5 Harness	0.42 [2] at 20C 0.38 at 320 C	0.24mm	Range: 900 – 1488 (Shi, 2014)

[1] Toray Cetex® TC1225: Product data sheet

[2] Prediction of effective thermal conductivities of woven fabric composites using unit cells at multiple length scale

Specific heat

In the study of Farkas the temperature-dependent specific heat capacity of a CF/peek composite was measured and calculated. The following plot is implemented in Abaqus with filling in the table.

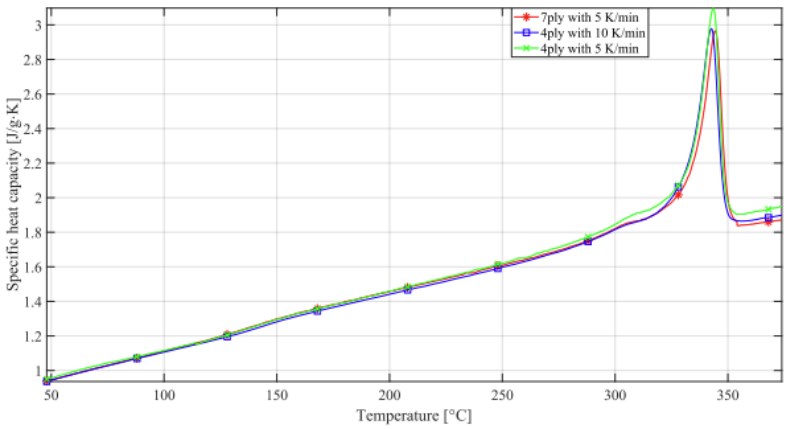

Figure 20: Best matches of the heat capacity results with different heating rates

Number of field variables: 0

Data

	Specific Heat	Temp
1	600	0
2	800	50
3	1000	70
4	1200	130
5	1300	150
6	1400	170
7	1500	210
8	1600	245
9	1700	275
10	1800	300

Model

SLS configuration in half– constant temperature at green arrows:

parameter	value	Unit
Interface temp	190 - 290	°C
convection	9 (Koenis, 2016)	W/m2k
Time	180	sec
Step size	0.5	sec

Figure 1 - Model with glass fiber – left side heat input

Results

Show not uniform surface temp.

Plotting following path for both situations:

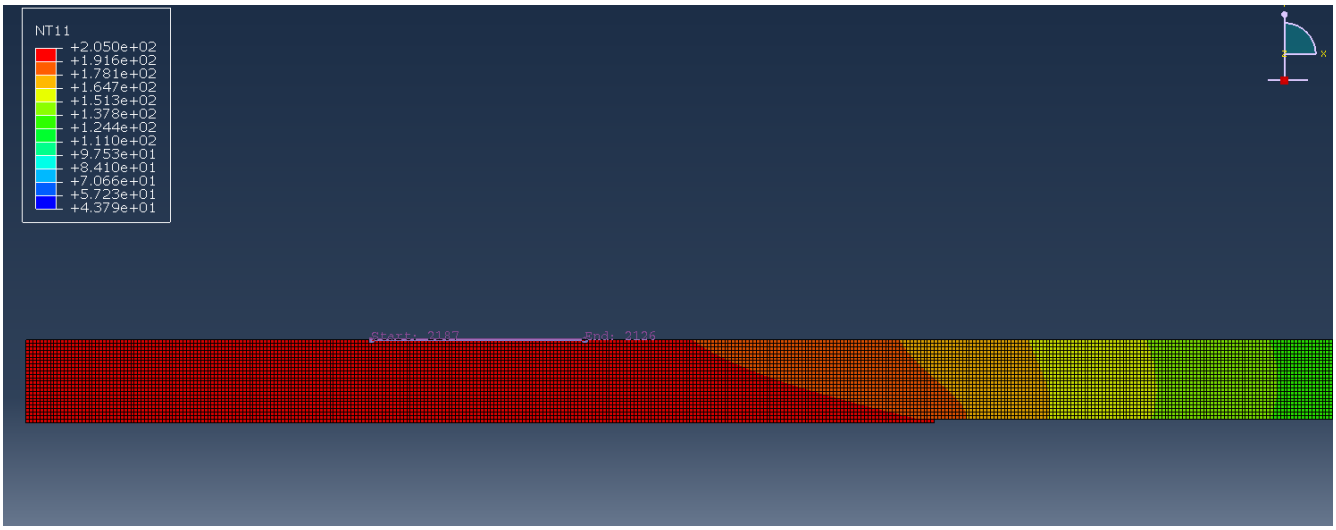

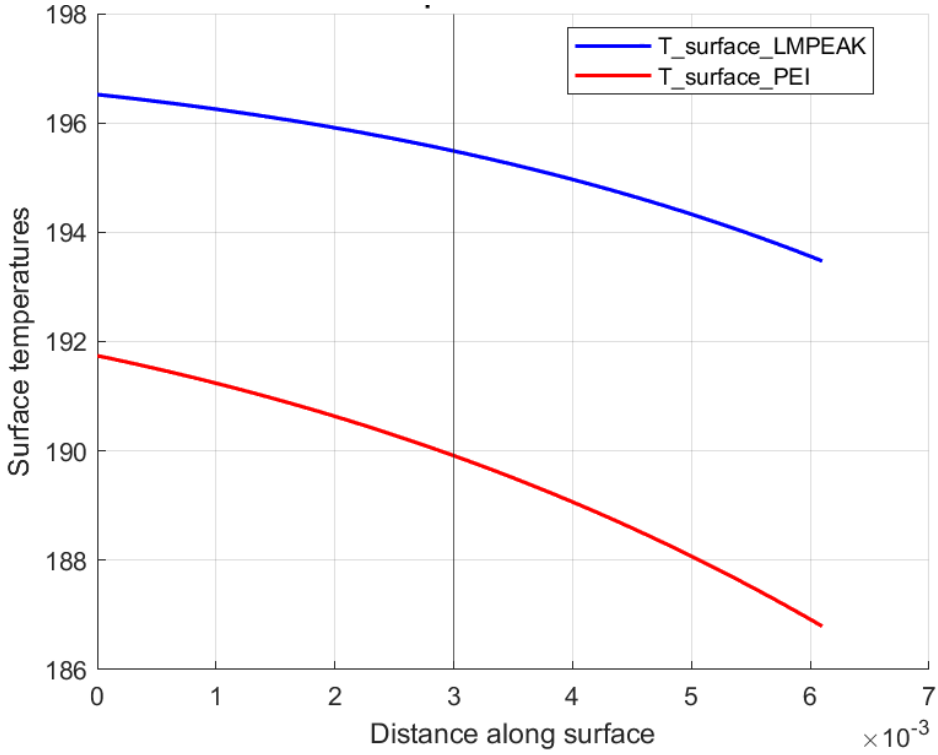

Figuur 1 – Abaqus result at interface temp of 225 Celsius, black line indicates the picked location for selecting the temp

Simulated temperatures:

Interface temp °C	**Average Surface temp °C**
190	**171**
210	**181**
235	**202**
260	**246**

B

Results welding

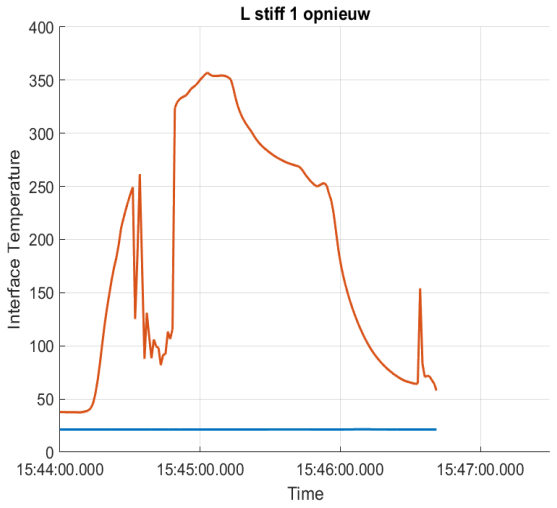
L stiff 1 opnieuw
Interface Temperature
Time
15:44:00.000
15:45:00.000
15:46:00.000
15:47:00.000

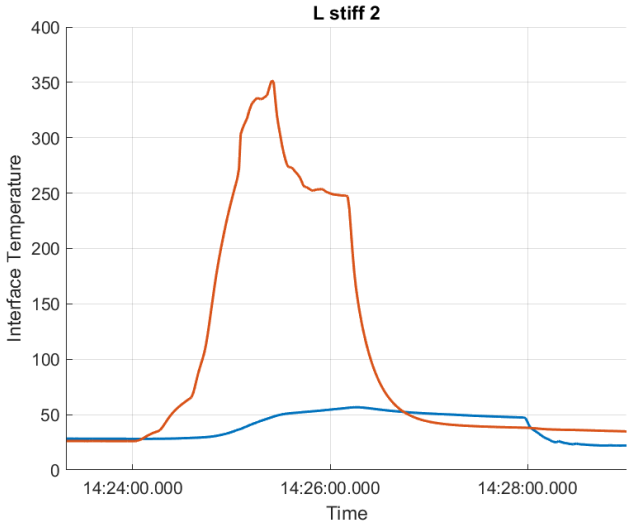
L stiff 2
Interface Temperature
Time
14:24:00.000
14:26:00.000
14:28:00.000

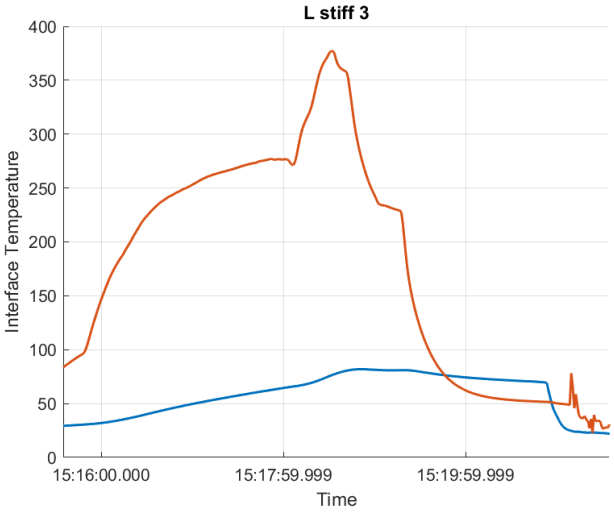
L stiff 3
Interface Temperature
Time
15:16:00.000
15:17:59.999
15:19:59.999

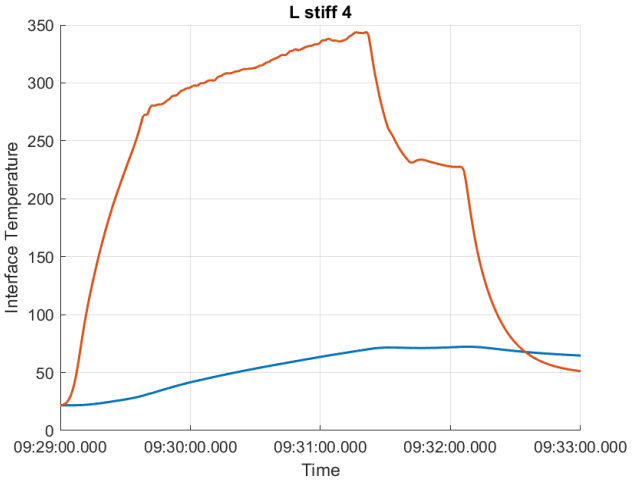
L stiff 4
Interface Temperature
Time
09:29:00.000
09:30:00.000
09:31:00.000
09:32:00.000
09:33:00.000

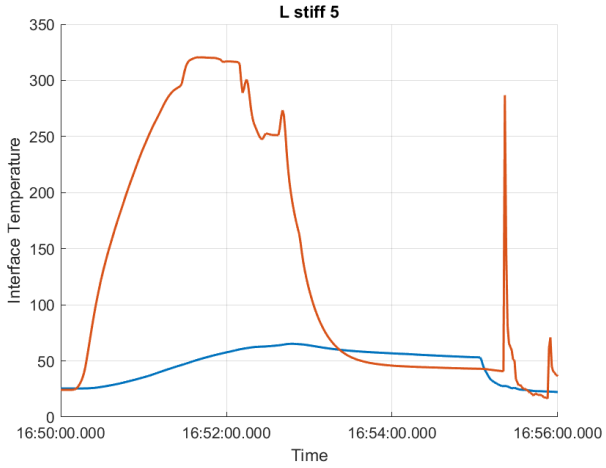
L stiff 5
Interface Temperature
Time
16:50:00.000
16:52:00.000
16:54:00.000
16:56:00.000

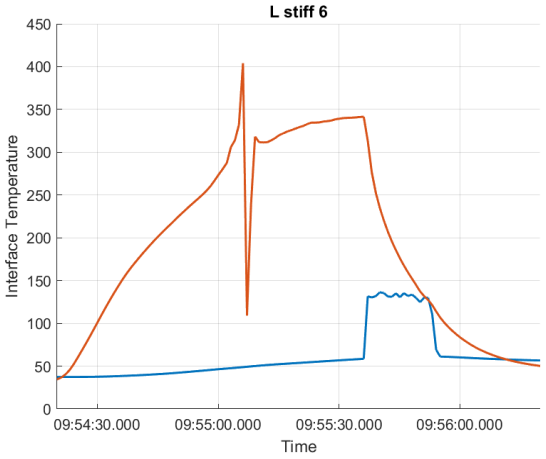
L stiff 6
Interface Temperature
Time
09:54:30.000
09:55:00.000
09:55:30.000
09:56:00.000

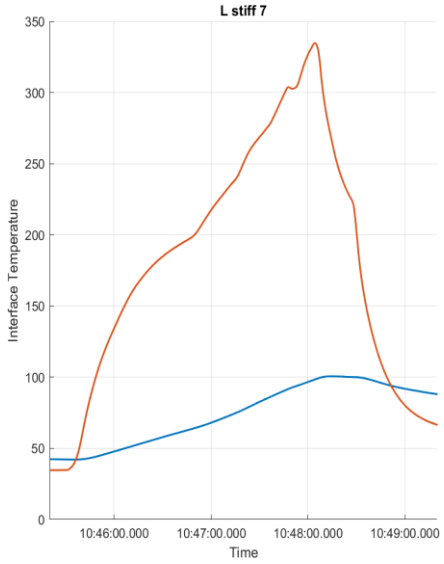
L stiff 7
Interface Temperature
Time
10:46:00.000
10:47:00.000
10:48:00.000
10:49:00.000

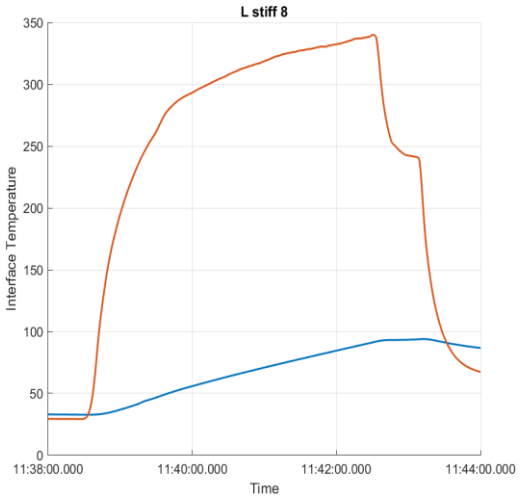
L stiff 8
Interface Temperature
Time
11:38:00.000
11:40:00.000
11:42:00.000
11:44:00.000

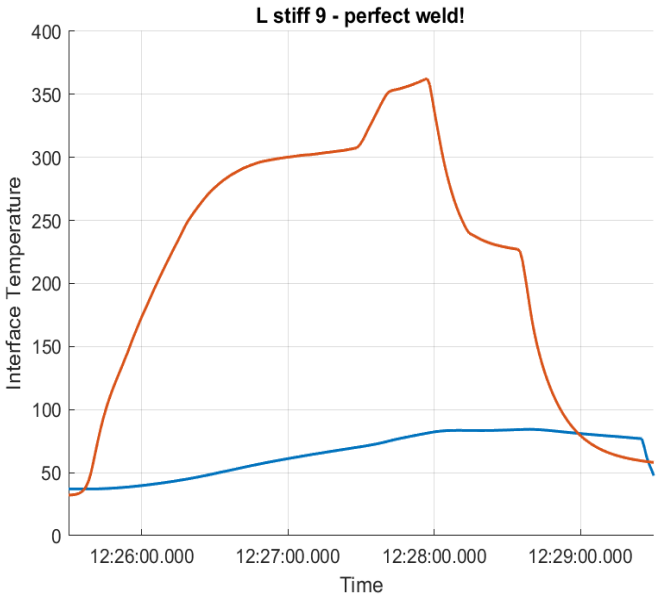
L stiff 9 - perfect weld!
Interface Temperature
Time
400
350
300
250
200
150
100
50
0
12:26:00.000
12:27:00.000
12:28:00.000
12:29:00.000

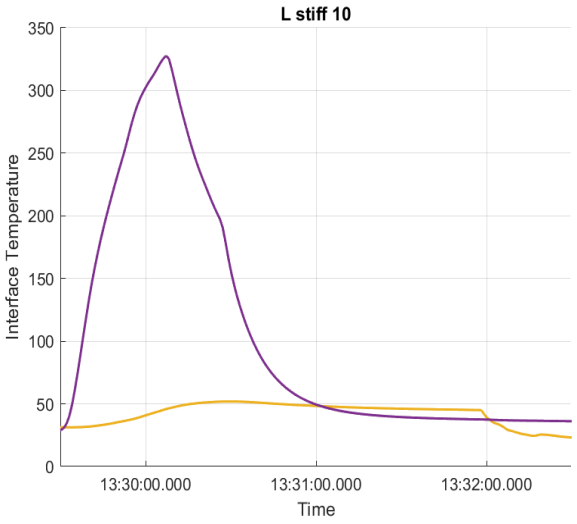
L stiff 10
Interface Temperature
Time
350
300
250
200
150
100
50
0
13:30:00.000
13:31:00.000
13:32:00.000

C

Sensitivity study

	Baseline values			T baseline
Symbol	Variable	Value	Unit	10%
Ky_glass	conductivity	0,2	W/mk	0,22
Ky_Laminate	conductivity	0,74	W/mk	0,814
		0,91	W/mk at 200C	1,001
Kx_Laminate	conductivity	6,4	W/mk	7,04
		9	wW/k at 200c	9,9
Rho_glass	Density	1920	Kg/m3	2112
Rho_laminate	Density	1590	Kg/m3	1749
alpha	convection coefficient	10		11
Q	heat density	-		
Cp_glass	Specific heat	1000	J/kg K at 50 C	1100
		2000	J/kg K at 275	2200
Cp_laminate	Specific heat	700	J/kg K	770
		900		990
		1050		1155
		1100		1210
		1300		1430
		1350		1485
		1450		1595
		1700		1870
		1800		1980

152.127 60sec!

Variable	effect on temp surf	Relative effect
ky_glass	152.218	**0,06%**
ky_Laminate	152.719	**0,39%**
kx_Laminate	150.532	**-1,05%**
ρ_glass	150.625	**-1%**
ρ_laminate	144.894	**-4,75%**
h	151.198	**-0,61%**
Cp_glass	149.714	**-1,59%**
Cp_laminate	144.060	**-5,30%**
q'''	162.060	**6,53%**

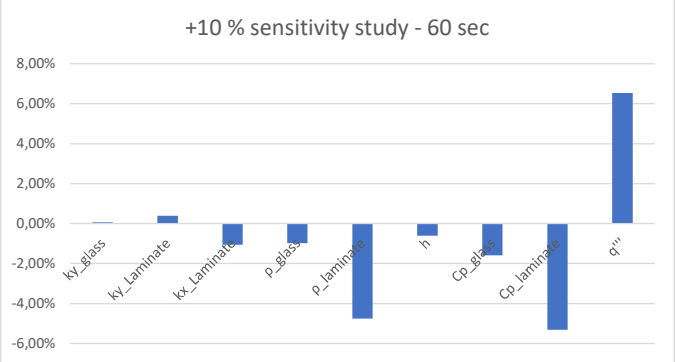

D

Plagiarism report

6% Overall Similarity

Top sources found in the following databases:

- 5% Internet database
- Crossref database
- 1% Submitted Works database
- 4% Publications database
- Crossref Posted Content database

TOP SOURCES

The sources with the highest number of matches within the submission. Overlapping sources will not be displayed.

1	**repository.tudelft.nl** Internet	<1%
2	**University of Twente on 2023-12-01** Submitted works	<1%
3	**Xuhai Xiong, Daosheng Wang, Jian Wei, Pu Zhao, Rong Ren, Jiapeng D...** Crossref	<1%
4	**coek.info** Internet	<1%
5	**mafiadoc.com** Internet	<1%
6	**Christophe Ageorges, Lin Ye, Meng Hou. "Experimental investigation of...** Crossref	<1%
7	**J. Barroeta Robles, M. Dubé, P. Hubert, A. Yousefpour. "Repair of ther...** Crossref	<1%
8	**Przemysław Dobrzański. "Bonding of High Temperature Thermoplastic...** Crossref	<1%

9	link.umsl.edu Internet	<1%
10	docstoc.com Internet	<1%
11	dokumen.tips Internet	<1%
12	ris.utwente.nl Internet	<1%
13	mdpi.com Internet	<1%
14	lirias.kuleuven.be Internet	<1%
15	D STAVROV, H BERSEE. "Resistance welding of thermoplastic composi... Crossref	<1%
16	eprints.soton.ac.uk Internet	<1%
17	info.pursuitcycles.com Internet	<1%
18	myprojecttopics.com Internet	<1%
19	modernonco.orscience.ru Internet	<1%
20	journals.sagepub.com Internet	<1%

21	elib.dlr.de Internet	<1%
22	export.arxiv.org Internet	<1%
23	hybrid2018.dgm.de Internet	<1%
24	escholarship.mcgill.ca Internet	<1%
25	repository.up.ac.za Internet	<1%
26	tel.archives-ouvertes.fr Internet	<1%
27	biblio.ugent.be Internet	<1%
28	link.springer.com Internet	<1%
29	ouci.dntb.gov.ua Internet	<1%
30	sciendo.com Internet	<1%
31	Gaoming Dai, Leon Mishnaevsky. "Fatigue of multiscale composites wi... Crossref	<1%
32	Harry Frederick, Wencai Li, Genevieve Palardy. "Disassembly Study of ... Crossref	<1%

33	hal.archives-ouvertes.fr Internet	<1%
34	Amanat, N.. "Welding methods for joining thermoplastic polymers for t... Crossref	<1%
35	Meng Hou, Mingbo Yang, Andrew Beehag, Yiu-Wing Mai, Lin Ye. "Resis... Crossref	<1%
36	espace.etsmtl.ca Internet	<1%
37	prism.ucalgary.ca Internet	<1%
38	spectrum.library.concordia.ca Internet	<1%
39	utwente on 2020-04-07 Submitted works	<1%
40	3d-sting.com Internet	<1%
41	Ismail Baha Marti, Cevdet Kaynak. "Effects of interlayer forms on the r... Crossref	<1%
42	M. M. Thawre, R. K. Paretkar, D. R. Peshwe, Ramesh Sundaram, C. M. ... Crossref	<1%
43	University of Twente on 2024-04-04 Submitted works	<1%
44	publikationen.bibliothek.kit.edu Internet	<1%

45	pubmed.ncbi.nlm.nih.gov Internet	<1%
46	scholar.lib.vt.edu Internet	<1%
47	amrita.edu Internet	<1%
48	peeref.com Internet	<1%
49	pes-publications.ee.ethz.ch Internet	<1%

Excluded from Similarity Report

- Bibliographic material
- Cited material
- Manually excluded sources
- Quoted material
- Small Matches (Less then 10 words)

EXCLUDED SOURCES

University of Twente on 2024-02-26

Submitted works

8%